Methods for Increasing Density of Binder Jet 3D Printed Tungsten Carbide-Cobalt

by

Katerina Kimes

B.S. in Materials Science and Engineering, University of Pittsburgh, 2017

Submitted to the Graduate Faculty of the

Swanson School of Engineering in partial fulfillment

of the requirements for the degree of

Master of Science

University of Pittsburgh

2021

UNIVERSITY OF PITTSBURGH

SWANSON SCHOOL OF ENGINEERING

This thesis was presented

by

Katerina Kimes

It was defended on

March 31, 2021

and approved by

Ian Nettleship, Ph.D., Associate Professor
Mechanical Engineering and Materials Science

Nikhil Bajaj, Ph.D., Assistant Professor
Mechanical Engineering and Materials Science

Thesis Advisor: Markus Chmielus, Ph.D., Associate Professor
Mechanical Engineering and Materials Science

Methods for Increasing Density of Binder Jet 3D Printed Tungsten Carbide-Cobalt

Katerina Kimes, M.S.

University of Pittsburgh, 2021

Tungsten-carbide cobalt (WC-Co) is a hard, tough, and wear resistant ceramic-metal composite that is commonly used in tooling applications and is produced using traditional powder metallurgy (PM) techniques. This production method causes limitations in part quantity, and complexity. As a result, binder jet 3D printing (BJ3DP) has been considered as an alternative to the traditional PM methods. Benefits of BJ3DP include decreased manufacturing time for complex parts, greater flexibility in part complexity and quantity, ease of use, and avoidance of thermally induced stresses common in other additive manufacturing methods. To feasibly implement BJ3DP into the current production process, there must be a greater understanding of the effects of printing parameters on the final material properties of WC-Co parts. This study addresses the optimization of BJ3DP parameters to achieve green and sintered densities comparable to traditionally manufactured WC-Co parts. The design of experiments method for process optimization was implemented to study first, the effects of powder spreading parameters on the powder packing rate, and second, the effects of binder printing parameters on green and sintered part densities. Mechanical and magnetic properties were also evaluated to gain an understanding of how parts produced via BJ3DP compare to parts produced using traditional methods. It was found that layer thickness and feed ratio are the most effective parameters in changing the density of the powder in the powder bed. Effects of printing parameters were difficult to conclude due to high standard deviations of green and sintered densities. However, certain parameter sets produced clearly better results than others. Additionally, it was found that the current BJ3DP process has the capability of

producing parts within acceptable density, hardness, and toughness limits for industry. Limitations of the process included poor green part strength and surface finish and is an area for further study.

Table of Contents

List of Tables

List of Figures

Preface

"Since we have gifts that differ according to the grace given to us, let us exercise them" – Romans 12:6

I am grateful for the gifts, knowledge, and experience I have received that were necessary to complete this work. Many of the gifts I have received take the form of those people who have helped me throughout my time in graduate school. I have been blessed to work with many talented, intelligent, and kind people that made the completion of this thesis possible. Among them are members of the Chmielus Lab group, especially Erica Stevens, Amir Mostafaei, Jakub Toman, Pierangeli Rodriguez De Vecchis, Danielle Brunetta, and Aaron Acierno. This work would have not been possible without the collaboration of our project partner, Drew Elhassid of General Carbide and the technicians who assisted with sintering and various tests. I'd also like to thank the professors, post-docs, and graduate students from various departments who helped out including: Dr. Ian Nettleship, Ahmed Talaat, Rafael Rodriguez De Vecchis, Dr. Sachin Velankar, Xianheng Guan, Nandan Pitre, Dr. Lei Li, Bingchen Wang, and Alan Tirado. Staff from the PINSE NFCF including Esta Ablev, Mike McDonald, and Dan Lamont, staff from the SCPI including Andy Holmes and Jeff Speakman, John Lemon and Brandon Blasko from the ANSYS AMRL at Pitt, and Liza Allison from Pitt UPCAM. Additional thanks go to technicians and engineers from ExOne including Matt Defibaugh, David Miller, Kyle Meyers, Andrew Klein, and Patrick Dougherty.

I'd also like to extend a much deserved thank you to my family and friends, who have been a constant source of support, encouragement, and love for me throughout my time in graduate school, namely: my parents Mark and Sharon and siblings Joshua and Kathryn, my boyfriend John,

dear friends Katrina, Liz, Carmelena, Greg, José, Juan, Hannah, and Matt, and many others whom I've shared memories with throughout graduate school, and Fr. Stephen for guidance in discernment. During graduate school, the Newman Catholic Graduate Student Association provided valuable growth in my faith, in relationship, and leadership that was imperative to my journey.

Among those who have journeyed with me throughout graduate school, I am especially grateful for the support, knowledge, sense of humor, and kindness of Dr. Chmielus. Since my time in the undergraduate program, he has welcomed me into his lab group, providing the environment to learn hands-on and technical knowledge that I would not have gained otherwise. Dr. Chmielus has taught me that we are all individuals in this journey and that it's okay that my path in graduate school does not look like everyone else's because it shouldn't. During a particularly difficult time along my journey, he described his role as an advisor by saying "I am here to help you get to the end you want." The selfless, caring disposition of Dr. Chmielus is what has helped me to push through to the end, learning more about myself than I ever thought I would in the process. Dr. Chmielus's friendship and advisement are truly a gift.

This project was financed by a grant from the Commonwealth of Pennsylvania, Department of Community and Economic Development.

Introduction

Tungsten carbide-cobalt (WC-Co) is a ceramic-metal composite commonly used in tooling applications due to its combination of high hardness and toughness and superior wear resistance to many other alloys. It has been produced using traditional powder metallurgy techniques since the first patents on the topic were published in 1923 [1]. Although this method has been viable for almost 100 years, there are limitations to the process that prevent parts with complex internal structures from being produced. Additionally, there are restrictions on part quantities due to the requirement of a specific mold for each different part that is produced. The advent of binder jet 3D printing (BJ3DP) provides an opportunity to change the trajectory of the WC-Co industry, allowing parts with complex geometries in specific quantities to be accurately and feasibly produced [2-4]. By repeating the process of spreading layers of powder and selectively depositing binder until a part is built, BJ3DP holds an advantage to other methods of additive manufacturing (AM) due to its scalability, cost-effectiveness, and lack of thermal stresses [3-5]. Although the BJ3DP of WC-Co has been considered by a number of researchers [6-9], there is still a gap in knowledge with respect to an understanding of how printing parameters effect the final part properties for WC-Co.

The high hardness and toughness of WC-Co are a result of the two main phases that make up the cermet: the hard ceramic WC grains and the tough Co metal matrix. The properties of the two phases combine to make a material with superior properties. Due to the presence of the metal matrix, liquid phase sintering drives the solidification of a powder part. During the sintering process, WC grain growth is controlled in order to control final properties. Fine- and ultra-fine-grained carbides are standard for quality parts but medium- and coarse-grained parts are also

produced. As in any new process, attention to the microstructure is important. It is important to avoid features such as excessive grain growth, Co pooling, eta phase, and graphite in the WC-Co microstructure. These undesirable features cause inconsistent properties and embrittlement. [1] Because BJ3DP is not frequently used in the WC-Co industry, the implications of process parameters on microstructure are not very well understood. The aim of this study is to develop a set of processing parameters to binder jet print WC-Co samples that have comparable properties such as density, microstructure, hardness, and toughness to those of traditionally manufactured WC-Co. This knowledge can contribute to the integration of BJ3DP into the manufacturing process of WC-Co, allowing manufacturers to more easily, rapidly, and cost-effectively produce parts with complex geometries not possible with traditional methods.

1.0 Background

1.1 Tungsten Carbide-Cobalt

Tungsten carbide-cobalt (WC-Co) is a type of ceramic and metal composite, known as a cermet. WC-Co is known for its high density, hardness, fracture toughness, and flexural strength, making it ideal for cutting tools, abrasives, and armor-piercing projectiles [10-12]. WC-Co consists of hard carbides, in this case tungsten carbide, in a matrix of a ductile metal binder (Co). The WC phase provides the high hardness and electrical conductivity [1, 13]. A wide range of properties can be achieved in WC-Co parts by tailoring the microstructure through the hard phase/metallic binder ratio and the processing parameters. The ability to tailor the mechanical properties of WC-Co makes it suitable for a wide range of applications [1].

WC-Co parts are traditionally produced via a pressing, extruding, or molding process followed by liquid phase sintering, allowing for parts to be made in many geometries, dictated by mold capabilities [1, 14]. The WC-Co powder is mixed with a plasticizer before forming to help parts hold their shape [15]. Powder compaction occurs at high pressures, resulting in a green part. Additional machining is often done on green parts to acquire geometries not achievable using a mold [1]. The green parts are then put through a pre-sintering and a final liquid phase sintering process. During sintering, molten cobalt is formed as a liquid phase and wets the surface of the WC grains, partially dissolving them [15, 16]. As the WC dissolves, it migrates and reprecipitates onto the surface of the original WC grain, creating a three-dimensional WC skeleton with Co as the binder matrix [13].

1.1.1 Powder Properties

Nanocrystalline WC-Co powder is the raw material used for the production of WC-Co hardmetal parts. The grain sizes of the WC in the powders plays a large role in the microstructure and properties of the final WC-Co parts [17, 18]. The powder is synthesized from nano-grained WC and cobalt metal using various methods including high-energy ball milling, in situ carburization, plasma synthesis, chemical synthesis, electroless plating, and spray conversion processes [17-20]. Despite the fine-grained nature of WC-Co powder, high-density final parts have WC grains on the micrometer scale due to the requirement of high temperature liquid-phase sintering [20].

In industry, spray conversion processes are commonly used. This method can produce high-purity powders with few steps while maintaining small WC grain size. The process starts with the preparation of a W, Co, and C mixed solution which is then spray dried to form precursor powders which are then put through a continuous reduction-carburization process whereby the nanocrystalline WC-Co composite powder is synthesized [15, 17]. The WC and the Co in the resulting powder are mixed on a molecular level, providing an amorphous carbide powder [15].

Another common method of powder synthesis used in industry is high-energy ball milling whereby elemental WC and Co are blended and ball milled over 10-120 hours. This method could potentially introduce contamination if the milling media is not made of WC-Co. The milling process helps to reduce the grain size of the WC by repeated deformation, fracture, and cold welding [18, 19].

To prepare the synthesized WC-Co powder for forming, the powder particles are agglomerated into larger spherical particles, typically between 15 and 45 μm, with a plasticizer, typically a wax [15, 21]. The resulting granules have enclosed pores [21] and very low density,

making them ideal for powder metallurgy techniques due to the ease of formability. However, in additive manufacturing, the low density of feedstock powder presents a challenge for obtaining high-density final parts. Figure 1 shows a comparison of the typical metal powders used for additive manufacturing, which are either spherical or irregular, and the spherical granules of WC-Co powder, which can break apart and are only held together by surface forces.

Figure 1. Various powder morphologies. WC-Co falls into the category of granules while many other powders used in additive manufacturing have spherical or irregular morphologies.

1.1.2 Microstructure

As previously mentioned, the WC-Co microstructure consists of tungsten carbide grains surrounded by a cobalt metal matrix minor phase (Figure 2), making it a unique class of material [1, 13, 22, 23]. WC-Co microstructures are typically described by the WC grain size and Co content and the part properties are greatly influenced by these two factors. Typically, the WC grain size is in the micrometer size range but can range anywhere from “ultrafine”, which is below 0.5 μm, to “extra course”, which is above 5.0 μm [13, 22]. Table 1 details the various categories of grain size identification [1, 24].

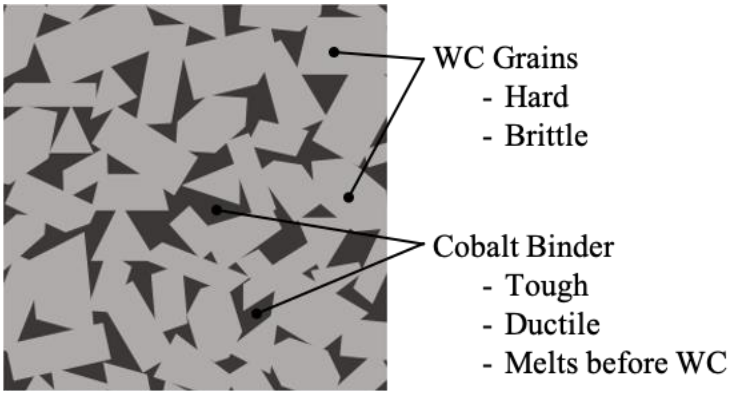

Figure 2. Illustration of a typical WC-Co microstructure. A tough cobalt binder surrouds hard tungsten carbide grains of sized ranging anywhere from 0.2 µm to >5.0 µm.

WC/WC contacts form a skeleton in the microstructure and the proportion of these contacts in the microstructure is known as contiguity [1, 25]. Various studies have been done linking the contiguity to the binder volume fraction and WC grain size. These relationships are necessary because binder volume fraction cannot simply be determined by the rule of mixture due to the presence of the WC skeleton [1, 26]. Typical cobalt binder content is between 2 and 18 wt.% [15]. The binder volume fraction is proportional to Co content and can be calculated from the mean free path of the binder and average WC grain size [1].

Table 1. Grain size ranges for WC grains [1].

Grain Size Designation	Size Range (µm)
Ultrafine	0.2-0.5
Submicron	0.5-0.9
Fine	1.0-1.3
Medium	1.4-3.4
Coarse	2.5-5.0
Extra Coarse	>5.0

WC-Co grain size and binder content determines properties such as edgeline toughness, bulk toughness, hardness, and thermal conductivity [1]. By decreasing WC grain size into the

micrometer scale, wear resistance and hardness is observed to increase. Upon decreasing grain size further into the nano scale, hardness, strength, and toughness can be further enhanced [15, 27]. As a general rule of thumb, hardness and wear resistance increase with decreasing grain size while toughness decreases with increasing Co content [1, 27, 28]. Both sintering parameters and cobalt concentration play a role in WC grain size and growth. A higher sintering temperature results in larger WC grains due to Oswald ripening and as cobalt is added, grain growth by recrystallization is inhibited resulting in smaller grain sizes [1, 15, 29].

Another method of controlling grain size is to add a grain growth inhibitor to the alloy which also changes WC grain shape. This is commonly an element such as V, Ti, Cr, Ta, Mo, or Nb which forms a carbide in the microstructure. Vanadium is the most effective grain growth inhibitor, but it can cause embrittlement when VC precipitates at WC grain boundary corners. Ti has been found to balance grain size in addition to inhibiting grain growth. Corrosion resistance can be influenced by the addition of Cr. The use of grain growth inhibitors and their effects are still not fully understood so there is a lot of study in this area of the field [1, 26, 30-32].

1.1.3 Phases

WC-Co ideally consists of two phases when C content of WC is close to 6.12 at. %: the hexagonal WC grains and the Co binder [11, 33]. However, depending on processing parameters, carbon can vary in concentration. This variance results in a third phase being formed. In the case of a carbon deficit, a brittle M_6C, η phase forms and in the case of excess carbon, soft graphite inclusions form [15, 22, 23, 34-36]. Presence of either of these phases are detrimental to material performance, making it useless for the desired applications [22, 37, 38]. Often times, the η phase forms as either Co_2W_4C or Co_3W_3C [39].

The η phase has two distinct morphologies, depending on carbon content and sintering temperature. In cases where sintering occurs in the WC + L + η region of the phase diagram (Figure 3), the η phase resents itself in a fine irregular shape. However, the η phase that forms from sintering in the WC + L region of the phase diagram shows dendritic growth which eventually grows into a large grain with an octahedral shape. This η phase is the M_6C type with varying composition and lattice parameter based on other alloying elements [40].

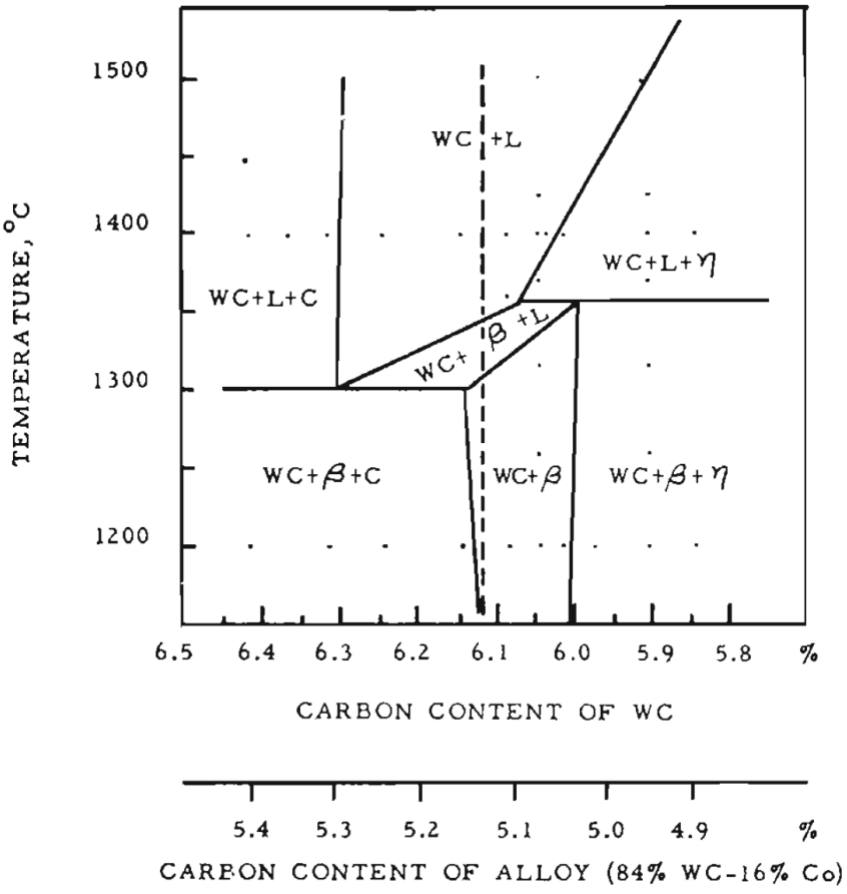

Figure 3. Phase diagram for a 16 at. % Co alloy [33]. Used with permission of The Minerals, Metals & Materials Society.

Eta phase forms during sintering when WC contains less than 6.00 at.% C. At this concentration, η phase will remain even at low temperature. However, if the concentration is

increased slightly to between 6.00 and 6.06 at. %, the η phase will present upon quenching. The η phase can be avoided at room temperature by controlled slow cooling, causing decomposition of the phase [33].

The sintering temperature and heating schedule also plays a role for alloys with C content between 6.00 and 6.06 at. % [33, 41, 42]. At temperatures around 1370 °C, the η phase is present in larger sections throughout the microstructure. However, upon increasing the sintering temperature closer to 1500 °C, the η phase precipitates along grain boundaries as a network [33].

Interestingly, it has also been shown that η phase presence is influenced by compaction pressure during forming operations [41, 42]. A higher compacting pressure causes less η phase to form and when cold isostatic pressing is used, no η phase is formed. The inverse relationship between compaction pressure and η phase formation is due to the reduction in free surfaces that occurs for samples compacted with higher pressure. By reducing the free surface area, the area that carbon is in contact with oxygen decreases, and the amount of carbon lost due to reaction with oxygen decreases. As a result, the C content is maintained and without a deficiency in C, η phase cannot form [41].

1.1.4 Mechanical Properties

WC-Co is such a widely used material due to its superior mechanical properties brought upon by the combination of hard carbide grains and tough metallic Co binder. The difficulty in tailoring properties of these materials stems from the inverse relationship between hardness and toughness: when hardness increases, toughness decreases, and vice versa [43, 44]. As a result, hardness and toughness are often measures of how well a material will perform in service [45].

This combination of hardness and toughness is benefitted by the WC/Co coherent boundary [16]. Indentation techniques are the most widely used methods of determining mechanical properties of WC-Co materials. Specifically, Vickers hardness and nanoindentation are commonly used [43]. It can be difficult to evaluate hardness of cemented carbides due to the brittle nature of the parent WC phase. Being that WC is ceramic, it exhibits little to no deformation under load, making it susceptible to cracking and spalling [46].

As previously mentioned, an increase in WC grain size results in a decreased hardness, following the Hall-Petch relationship [41, 45, 46]. A superior hardness is therefore observed in parts with microstructures comprised of nano-sized grains, leading to a high volume fraction of grain boundaries [41]. Also influencing the mechanical properties and wear resistance of WC-Co parts are the composition, mainly the binder volume fraction of the alloy, the binder mean free path, and the carbide grain size. Therefore, by decreasing Co content, the binder mean free path decreases, and the hardness will increase [47].

Toughness is commonly determined in WC-Co alloys by analyzing the linear relationship between crack length and load. This method originated from the initial method by Palmqvist whereby crack lengths from the four corners of a Vickers indent were summed. In general, there is a linear dependence of indentation load on crack length, lending to the relationship between hardness and toughness in WC-Co alloys [47].

It is important to note the type of crack that forms when evaluating toughness. When indented with a Vickers tip, as done in this experiment, either radial median or a Palmqvist cracking can occur (Figure 4). Radial cracks occur from the corners of the indent and when they are large enough to combine under the indent, they form a radial median crack. When the surface containing the indent is polished, the crack can still be seen connected to the indent corners. On

the other hand, when the cracks remain separate, they are called Palmqvist cracks and upon further polishing, will be detached from the indent corners. The crack type ultimately determines which equations and constants to use for calculating toughness. Typically, WC-Co exhibits Palmqvist cracking. [48, 49]

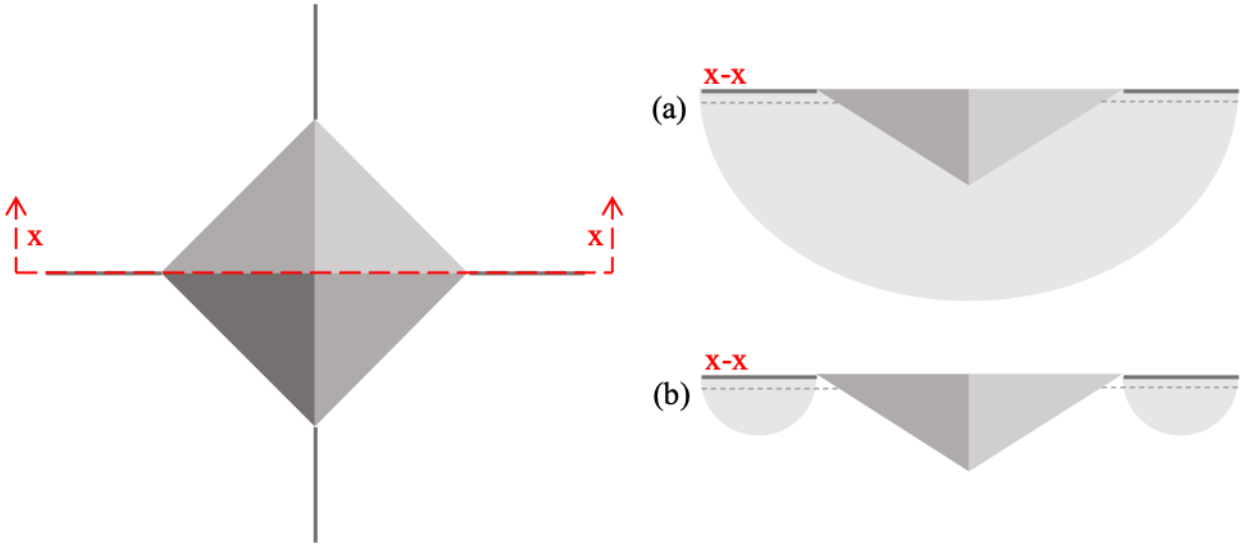

Figure 4. When an indent is made in WC-Co that induces cracking, either (a) radial median or (b) Palmqvust cracking occurs.

1.1.5 Magnetic Properties

As discussed previously, carbon content is crucial to the overall performance of WC-Co alloys. It can be difficult to measure carbon content accurately due to the lack of sensitivity or precision of many instruments for low carbon content materials. As a result, the magnetic properties, specifically magnetic saturation and magnetic coercivity, are commonly used to indirectly estimate the carbon content and grain size, respectively [1, 50-53].

Carbon content can be estimated from magnetic saturation, quantitatively, because it gives an estimate for how much W is dissolved in Co. The saturation is related to the composition of the

ferromagnetic Co binder phase. In turn, the overall C content can be determined. The magnetic coercivity is qualitatively related to the cobalt content mass fraction, along with average grain size [50-53]. There has been some disagreement in literature of the relationships between coercivity and grain size, mainly because of the use of different values to report average grain size. The differences arise from some studies using the mean linear intercept and others using the median linear intercept. The most important detail for comparing coercivity values is matching alloy grade [53].

Often times these magnetic measurements are used for quality control in industry [51, 53]. For any given grade of WC-Co there are expected values of magnetic saturation and coercivity which can be used as a standard when evaluating part quality during production [51]. Magnetic saturation typically increases as the amount of W in Co solid solution decreases [1]. Because coercivity is used to measure grain size, it can be compared to hardness measurements to find any inconsistencies as well [51]. In general, higher coercivity corresponds to smaller WC grain sizes and increases linearly with a decrease in grain size [1, 52]. Figure 5 shows how magnetic properties change based on phases and grain size.

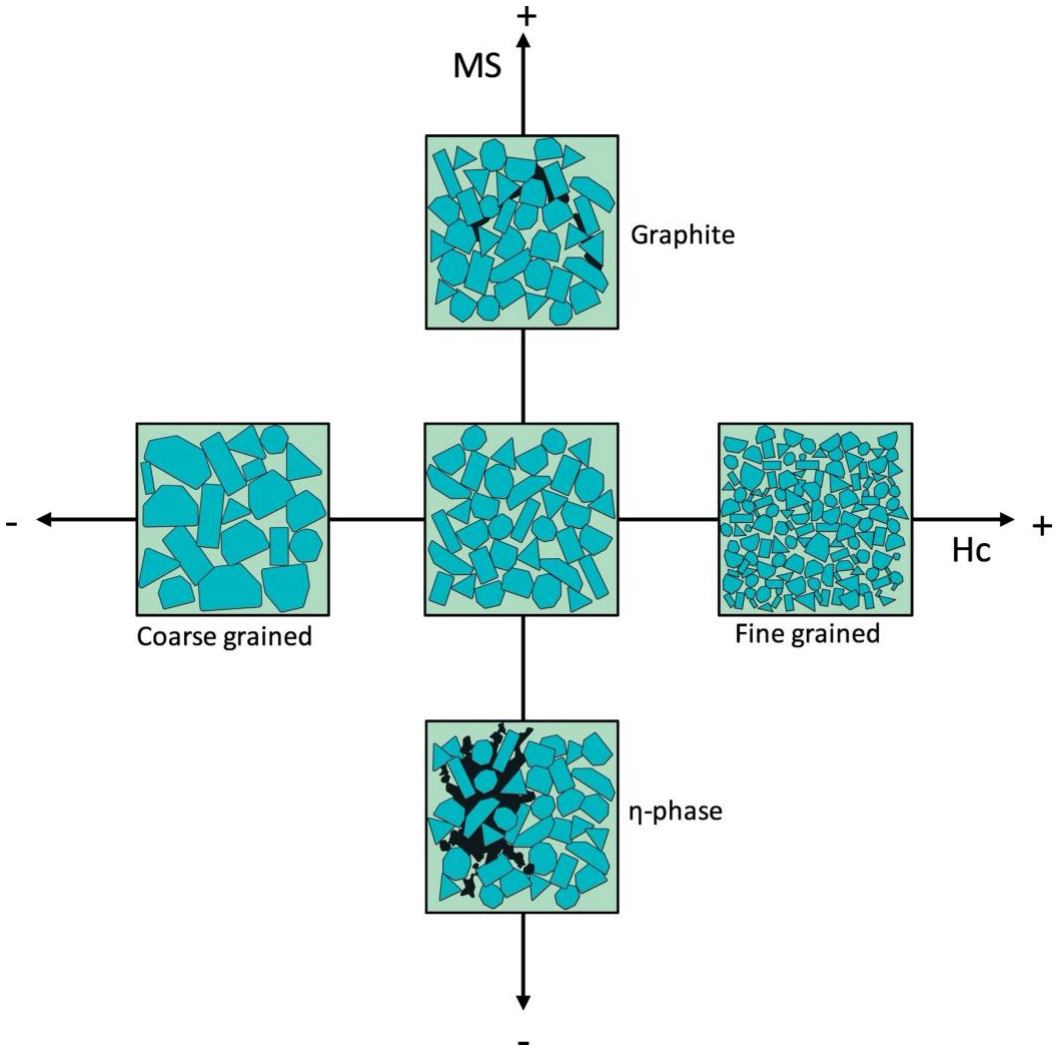

Figure 5. The effect of grain size and phases on the magnetic properties of WC-Co parts [1].

1.1.6 Traditional Manufacturing Process

Common methods of producing WC-Co parts are die pressing and powder injection molding (PIM) [36, 54-56]. Die pressing (Figure 6) is a method of shaping powder where powder fills up a mold cavity and is then placed under high pressure to compact the powder into a dense green part which is then ejected from the mold. PIM, often preferred to die pressing due to its versatility in part geometry, is a method of powder forming where hydraulic pressure is applied to

inject a powder and polymeric binder mixture in a mold or die. The powder fills up the mold cavity and is compacted into a dense green part, held together by the plasticizer [14, 54]. In both processes, the green part is then machined, if additional geometries are desired, debound, and sintered to achieve a fully dense final part [8]. Even with PIM there are limitations to part geometry and internal features. Additionally, a custom mold must be produced for any new parts.

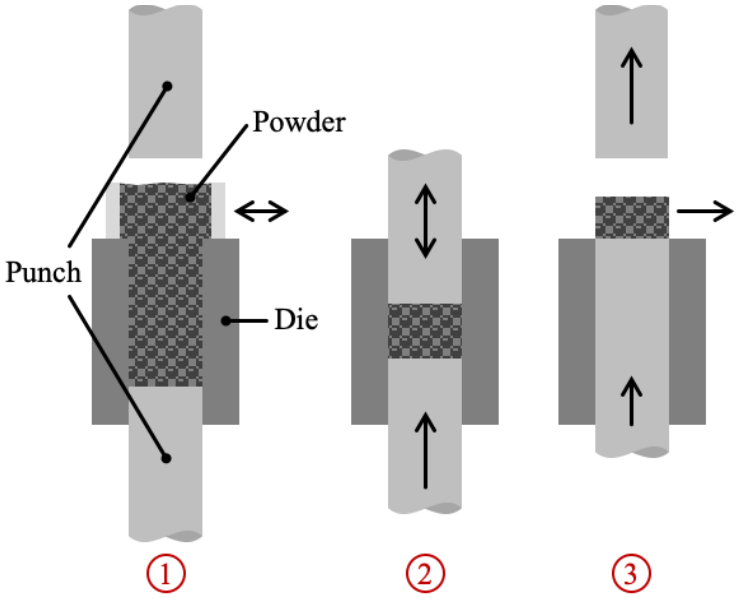

Figure 6. Die pressing process: (1) Die filling (2) Compaction (3) Green part ejection

Sintering can be completed via methods such as liquid phase sintering, sinter-HIP, or gradient sintering. HIP (Hot Isostatic Pressing) is a method used to densify powder parts by applying high isostatic pressure at high temperatures (Figure 7) [4, 57]. The pressure is applied using an inert gas and aids in the removal of pores while not negatively affecting the microstructure. By using HIP, the mechanical properties are improved and the reliability of the parts is more consistent [57].

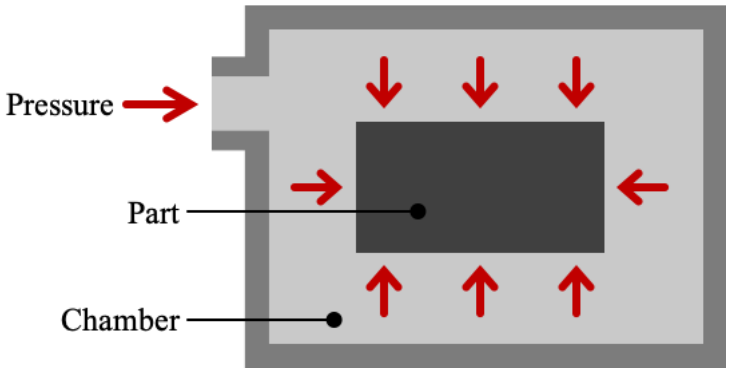

Figure 7. Schematic of a HIP process. The chamber containing the sample is pressurized with an inert gas where it aids in part densification during heating.

1.1.7 Industrial Applications

When WC was discovered in the 1920s, it was used primarily as wire drawing dies and cutting tools. Today, they are integral to the tool machining industry, having applications in chipless forming, mining, industrial wear parts, knives for paper, plastic, or textiles, and machining of metallic and non-metallic materials, to name a few [58].

Application depends on hardness and toughness, which in turn depend on grain size and cobalt content, as previously discussed. Figure 8 shows various WC-Co industrial applications and their respective properties.

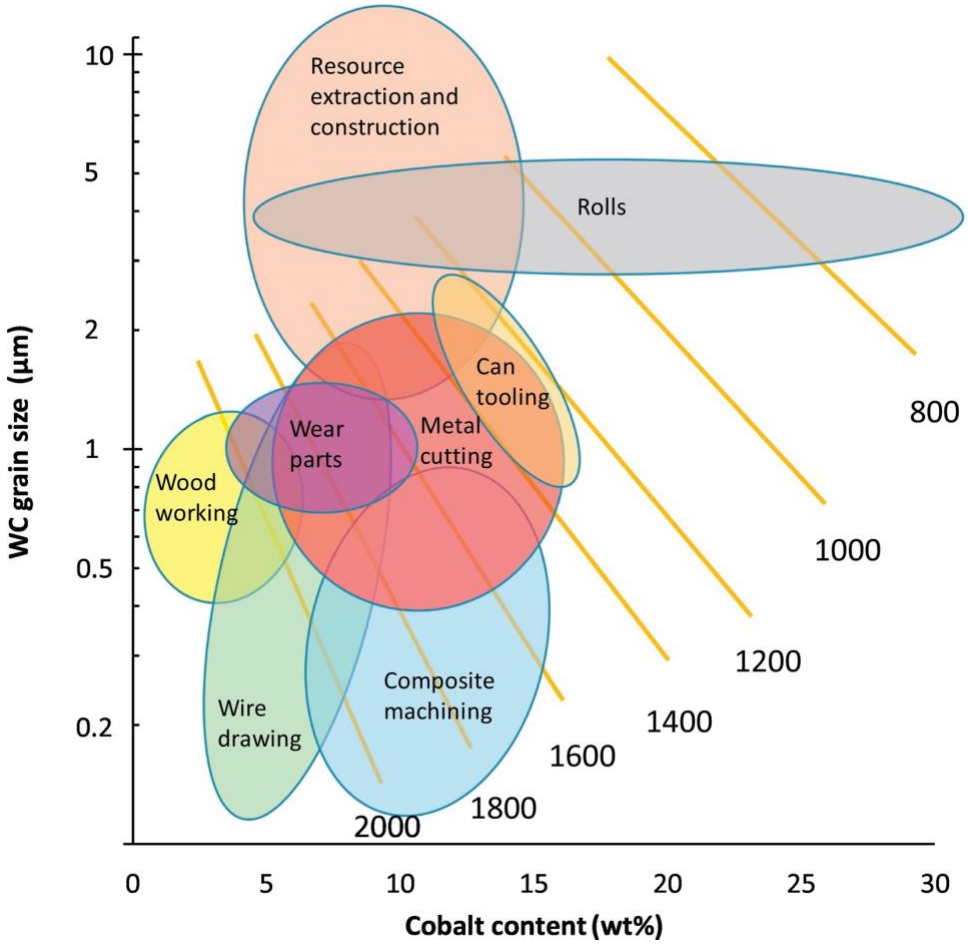

Figure 8. Industrial applications of WC-Co, based on grain size and Co content. Vickers hardness lines are shown [1].

1.2 Additive Manufacturing

Additive manufacturing (AM) is a fabrication method that has gained significant ground in recent years. Also known as 3D printing, AM builds parts layer by layer through methods such as extrusion, welding, curing, and inkjet deposition, among others. AM allows for small batches of highly complex parts to be built without need for intensive post-processing such as machining.

This not only eliminates the need for custom tooling or machine components, but it also eliminates material waste. AM also drastically reduces the cost and time needed to produce a part [5].

Parts are printed from computer-aided design (CAD) models. The most common methods for the AM of metals and cermets are welding and curing methods. In welding methods, a heat source is used to fuse raw materials together: the feedstock typically in the form of metal wire or powder. In curing methods, a liquid binder is used to selectively glue powder particles together layer-by-layer. This process requires no heat or special atmosphere [5, 59].

In the manufacturing of WC-Co, additive manufacturing (AM) technologies have been introduced as alternative processing methods [3, 5, 7-9, 60]. Among the many AM technologies, mainly laser-based welding methods such as selective laser melting (SLM) or selective laser sintering (SLS) have been studied. There has been some success in printing WC-Co using these methods, however, there are many problems arising from the processing method that make SLS/SLM impractical for manufacturing applications with the current capabilities. Common problems include low densities (40-70%), warping, delamination of layers, embrittlement, non-equilibrium phases, and thermal cracking [60, 61]. Because of these issues in using laser AM to process WC-Co, binder jet 3D printing (BJ3DP) has emerged as a potential alternative to the traditional powder metallurgy manufacturing methods.

1.2.1 Binder Jet 3D Printing

A schematic of a binder jet printer is shown in Figure 9. These printers build parts by using a liquid bonding agent to selectively bind a thin layer of powder. This powder spreading and binding process is repeated until the part is built. Post-printing, the parts are cured to strengthen

the green part. Green parts are removed from the powder and densified by either sintered in a furnace or infiltration [5, 59, 62].

The detailed printing process is as follows [5, 59]:

1. A digital CAD model of the part is sliced into thin layers and saved to an STL file.
2. The hopper or feed box and roller (see Figure 9) are used to deposit and spread a thin layer of powder onto the surface of the build box. The roller spins opposite the direction of translation and aids in loosely compacting and smoothing the powder surface.
3. A liquid binder is selectively deposited from a series of jets on a printhead, similar to an inkjet printhead. The amount of binder that is deposited is determined by the binder saturation, calculated from estimated powder bed density and input by the user.
4. To dry the binder, a heater (not shown in figure) passes over the powder bed. This step is necessary to prevent any disruption of the surface during spreading of the next layer. It also prevents any bound powder from sticking to the roller during the next layer spread.
5. To prepare for the next layer, the piston lowers the powder bed a distance equivalent to the layer thickness (typically 50-200 μm).

There are many advantages to this method of AM compared to the energy-based methods for printing metals and ceramics. BJ3DP has the capability of printing virtually any powdered material feedstock with a high build rate, compared to other methods. Many energy-based methods require slow scan speeds, leading to low production rates. Because BJ3DP only requires the movement of a printhead to bind powder, it is capable of higher production rates. Additionally, by eliminating the intensive heat source for melting layers of powder in an energy-based method, the final BJ3DP parts do not have residual stresses caused by variable cooling rates. BJ3DP has

advantages when it comes to stability and ease of part removal. Because parts are cured while still in the powder bed, no support structures are required for part stability during printing of overhangs or internal structures. The parts can easily be removed from the powder bed following curing without any additional processes, such as cutting a part off of a substrate. In energy-based methods, the parts are built directly onto a metal substrate and must be cut off, often times using a wire EDM, which can introduce even more heat-induced stresses and even cause cracking. Lastly, BJ3DP has the advantage of producing functionally-graded and porosity controlled parts [5, 59].

One drawback to BJ3DP is that printed and sintered parts often have a rough surface finish, leading to further post-processing in some cases. The surface finish is affected by the powder size and layer thickness where thin layers with small particles leads to smoother surfaces on the final parts. However, as the particle size decreases, the inter-particle forces increase and the ability for the powder to flow easily becomes an issue. This can cause difficulty in powder deposition and spreading [5, 59]. Bimodal powder distributions have been shown to result in layers that are packed better, leading to a denser final part [5, 59].

Some other drawbacks of BJ3DP include the need for post-processing steps because it is a multi-step process, low green densities resulting in distortion of parts during sintering, and high shrinkage rates. These drawbacks have been heavily researched in recent years and continue to be an area of development in BJ3DP [5].

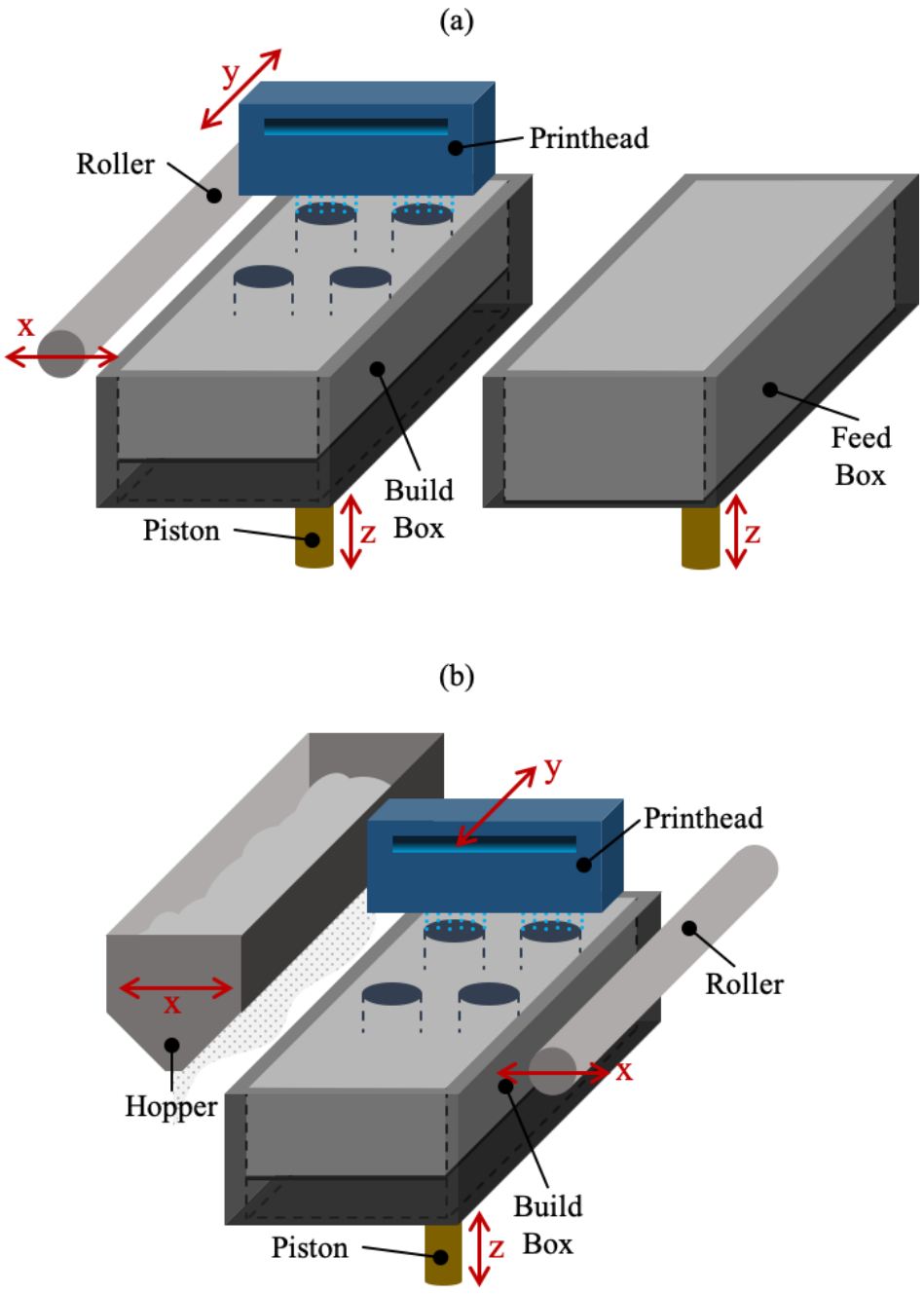

Figure 9. Schematic of a binder jet 3D printer that feeds powder via (a) a feed box and (b) a hopper.

1.2.1.1 Printing Parameters

During printing, there is a set of parameters that the user has control over. These parameters influence the quality of the build and the final part properties. The parameters are generally

optimized for the material, powder size, and desired final properties such as density and surface finish. For the purposes of this project, only parameters related to BJ3DP with a hopper (Figure 9b) will be discussed. These parameters include layer thickness, binder saturation, dry time, roller traverse speed, and feed ratio. Other parameters exist such as hopper oscillation speed, spread speed, and roller rotation speed but are not the focus of this study.

Layer Thickness **–** The layer thickness is a measure of how much powder is deposited onto the powder bed in the Z-direction for a single layer. The layer thickness typically falls between 15 and 300 μm for BJ3DP and is determined based on desired resolution and powder size. The layer thickness should be higher than the largest particle size for proper powder flow and spreadability [5]. Part density is also affected by layer thickness where a smaller layer thickness yields higher part density, so long as the powder size is sufficiently small [59].

Binder Saturation **–** This is a value that is calculated based on powder bed density, as seen in the following equation:

$$S = \frac{1000 \times V}{\left(1 - \left(\frac{PR}{100}\right)\right) \times X \times Y \times Z} \qquad \textbf{Equation 1}$$

where S is the theoretical binder saturation [%], V is the binder drop volume [pL], PR is the packing rate [%], X and Y are binder droplet spacings [μm], and Z is the layer thickness [μm] [5, 63].

The binder saturation is an important parameter because it affects the accuracy of the final part. A saturation that is too low will cause delamination of the printed layers and an increased number of voids in pores in the part. If a part is printed with the saturation being too high, on the other hand, there is a possibility for high surface roughness and dimensional inaccuracies [5, 63]. Binder saturation is often determined through trial and error but can also be determined through a more methodical approach using models or optimization studies [59].

Dry Time – This parameter defines the amount of time that the jetted powder surface is exposed to a heat lamp. The dry time aids in first, drying the binder, and second, partially curing the binder. With a proper dry time, subsequent layers can be printed without disruption of the previous layers. The dry time depends on the following factors: binder saturation, binder composition, layer thickness, how well the binder wets the powder, and powder bed characteristics (packing density, thermal conductivity, etc.). The dry time is also influenced by the power ratio of the heating element. It must be sufficiently high in order to dry the binder enough. A dry time that is too low insufficiently dries the binder and can result in disrupted layers and poor dimensional accuracy. Appropriate drying times act as a barrier for excessive binder migration into lower layers. This restricts binder saturation to the current layer of loose powder, thus aiding in dimensional accuracy. Therefore, it is important that the dry time and saturation level are appropriately matched to achieve well-built, dimensionally accurate parts [5].

Roller Traverse Speed – The speed at which the roller translates across the powder bed while the roller is spinning is known as the roller traverse speed. This parameter is part of the powder spreading process. The overall speed of the print is directly affected by the roller traverse speed and can therefore play a role in determining how long a build takes. The roller traverse speed can influence the consistency of the build. Inhomogeneous powder beds, leading to layer delamination, can result from roller traverse speeds greater than 4 mm/s [5, 64]. In general, slower speeds are better for this parameter but this comes at a cost of production speed [65].

Feed Ratio – A measure that is linked to roller traverse speed is the feed ratio. Both play a role in the overall packing density of the powder bed. The feed ratio is defined as the thickness of feed layer/layer thickness and is mainly a parameter of interest in machines that use a feed box to

feed powder. The feed ratio has been found to be a critical parameter for powder-binder interactions and densification, which are improved when a higher ratio is used [65].

1.2.1.2 Curing and Sintering

Both curing and sintering are post-processing steps necessary for the strengthening and densification of printed parts. Once printing has finished, the fragile green part is embedded in a bed of unbound powder. To strengthen the green parts enough to be able to remove them from the powder bed, the entire powder bed (embedded green parts and loose unbound powder) must be cured at a low temperature. This step depends on the binder chemistry and, in the case of the polymer-based binders used in this study, is necessary to complete binder crosslinking and polymerization [5, 59, 66]. Curing usually occurs between 180 and 200 °C for about 8 hours. After this step, the powder particles have still not fused together but are strong enough to be gently handled. As a result, the parts are very fragile [5].

Once parts are cured, they can be depowdered. The process of depowdering consists of carefully removing the cured green parts from the loose powder and any excess powder from the parts. This is achieved using a brush, compressed air, vibration, or a vacuum [5].

After parts are removed from the excess powder, they can be sintered. Sintering is a post processing heat treatment step where parts are densified and strengthened through diffusion. The density of the final part can be controlled during sintering by temperature and sintering time. Often times, a binder burnout step is included during the ramp-up to the sintering temperature. The burnout allows for pyrolysis of the binder, removing the volume of binder from the part and aiding in densification. During burnout, a carbon residue is typically left behind and can alter the composition or phases of the final part. After burnout, the temperature increases to reach the sintering temperature. The kinetics of sintering, and therefore the densification of the part, depend

on the following factors: powder chemistry and surface activity, powder morphology, particle size distribution, and sintering atmosphere. Therefore, the powder properties must be taken into account when designing a sintering procedure. The two main types of sintering that can occur are solid state sintering and liquid state sintering [5, 59, 62]. Materials like WC-Co go through liquid phase sintering (LPS) [67]. In this type of sintering, a liquid is formed at the sintering temperature and wets the surrounding particles. The process can be broken up into three stages: (1) rearrangement due to the formation of liquid between particles, (2) solution reprecipitation at contact points whereby maximum densification can be achieved, and (3) coalescence where a solid-state skeletal network forms, slowing densification [5, 59, 62]. Ultimately, the final part can reach full density, depending on the green density, sintering parameters, and particle interactions.

1.3 Design of Experiments

Design of Experiments (DOE) has been around since the 1920s and is employed in many process optimizations to help understand key variables in a reduced amount of time. The planning, designing, and analyzing of an experiment, with integrated statistical methods, make up the DOE process. In optimization experiments with many variables, it is a time consuming and difficult task to accurately assess all combinations and determine the interaction between variables in a time-efficient manner. The ultimate goal in applying DOE to process optimization is to reduce the variation that ultimately exists in all processes. DOE is based in statistical thinking and is driven by this idea to reduce variation to improve quality [68].

In DOE, the focus is on the inputs and output of the process. The inputs, or machine variables, are known as “factors” and these factors are randomized, replicated, and blocked in a

strategic manner to develop the statistically significant experiment. Factors can be varied at different values, or "levels". Randomization helps to reduce any experimental bias by removing sources of extraneous variation and gives each factor the same chance of being affected by non-controllable "noise" factors. Replication takes the entire experiment, or a portion of an entire experiment, and repeats it under more than one condition. By going through this process, it allows for experimental error to decrease and to more precisely identify the interaction effects. The downside to replication is that it extends the time and cost of an experiment. Lastly, blocking is used to improve the efficiency of experimental design by eliminating the effects of variation due to noise factors. Blocking groups are sets of similar or homogenous runs. The important thing to note with blocking is that it is important to eliminate variability between blocks from the experimental error [68].

The number of independent comparisons that can be made from a set of data is the number of degrees of freedom for the experiment. In DOE, the degrees of freedom of a given process variable is one less than the number of levels of that factor. For instance, if biner variation was varied with three levels (e.g. 80%, 100%, 120%), then there would be two degrees of freedom for that factor [68].

In DOE, there must be a measurement system in order to be able to compare effects. The measurement system is most effective when the system is based on a quality control variable [68]. In the case of BJ3DP, something such as green density or powder bed density can be used. This measurement must be able to be accurately measured and have an associated margin of error within an acceptable range [68].

1.3.1 Full Factorial Designs

Full and fractional factorial designs are among the most common experimental designs used in manufacturing. For the purposes of this project, the focus will be on full factorial designs. Joint effects of factors of the outcome of a process can be studied with factorial designs, which can be at either 2- or 3-levels. All possible combinations of levels for all factors are studied in full factorial designs where, for a 2-level design, 2^k total number of experiments are run, where k is the number of factors [68]. A 2^3 full factorial experiment design would have 8 total runs and the three factors would be have two levels each. A 3^2 full factorial design would have 8 total runs with two factors at three levels each.

1.3.2 Main Effects Plots

To compare the relative strength of design parameters and process variables, a main effects plot is used. The plot consists of the mean response values at each level of a design and shows if the response value responds in a negative or positive direction. The response is determined by the increase or decrease of the average responses and the strength of the effect, which can be observed from the slope of the line. Figure 10shows an example main effects plot for saturation on green density at two levels [68].

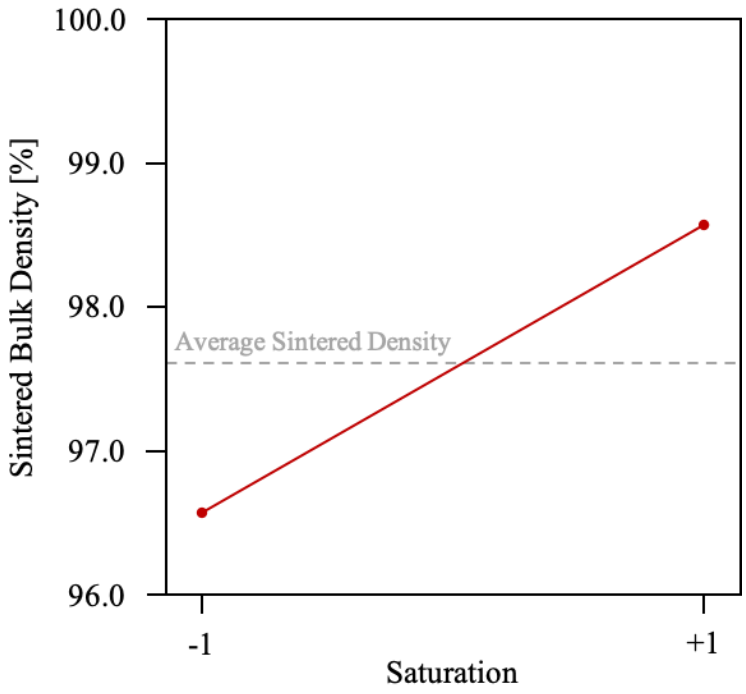

Figure 10. Example of a main effects plot for the effect of binder saturation on green density.

In the example above, the saturation has a positive effect because the average response at the high level is that than the average response at the lower level. The strength of the effect can be compared to other effects by determining the slope. The effect of the saturation can also be calculated using the following equation:

$$E_f = \bar{F}_{(+1)} - \bar{F}_{(-1)} \qquad \textbf{Equation 2}$$

where E_f is the parameter effect, $\bar{F}_{(+1)}$ is the average high-level response, and $\bar{F}_{(-1)}$ is the average low-level response of the factor [68].

2.0 Research Description

2.1 Hypotheses

1. WC-Co parts can be produced using BJ3DP that fall within acceptable ranges for the following properties:
    a. Grain Size
    b. Density
    c. Hardness
    d. Toughness
2. A set of printing parameters can be developed to optimize green and sintered density for WC-Co parts using the design of experiments (DOE) method.

2.2 Objectives

1. Develop a set of powder spreading parameters (roller traverse speed, feed ratio, and layer thickness) using DOE to achieve a powder packing rate comparable to tap density.
2. Determine a set of printing parameters (binder saturation and dry time) using DOE to achieve sintered densities comparable to traditionally manufactured part densities.
3. Evaluate the microstructure (grain size, phases), mechanical properties (hardness and toughness), and magnetic properties to compare to traditionally manufactured WC-Co.

3.0 Experimental Methods

3.1 Powder Characterization

After preliminary testing on as-received powder and heat-treated powder, it was determined that heat-treated powder would produce the strongest green parts. Heat-treatment of the powders was used to remove the plasticizer from the powder particles which allows the binder used in BJ3DP to adhere more effectively to the powder. No particle sintering occurs during powder heat-treating. Table 2 shows a list of the 13 powders that were received from General Carbide and analyzed to determine which would be best for printing.

Table 2. List of powders from General Carbide that were analyzed.

Powder Name	**Type**	**Co Content (wt. %)**	**Post-Processing**
GC03_A	Vacuum Dried	3	
GC15_A	Vacuum Dried	15	
GC25_A	Vacuum Dried	25	
SP03_A	Spray Dried	3	
SP15_A	Spray Dried	15	
SP25_A	Spray Dried	25	
GC03_B	Vacuum Dried	3	Heat-Treated
GC15_B	Vacuum Dried	15	Heat-Treated
GC25_B	Vacuum Dried	25	Heat-Treated
SP03_B	Spray Dried	3	Heat-Treated
SP15_B	Spray Dried	15	Heat-Treated
SP25_B	Spray Dried	25	Heat-Treated
SP313_C	Spray Dried	13	Heat-Treated, Smaller Distribution

Flow Tests **–** Flow tests were done for the seven spray dried powders to get flow characteristics according to ASTM B215, Method 2. Vacuum dried powders do not flow at all, so there was no need to perform tests. A Hall Flowmeter funnel (Figure 11) was used with 50 g of powder. The powder was loaded into the flowmeter funnel without tapping or vibration. The timer was started when the powder began to exit the orifice and the time it took for the powder to flow completely into the density cup was recorded. If the powder did not flow or got stuck, one tap on the side of the funnel was allowed but further tapping was not allowed. The timer was stopped when the last bit of powder exited the flowmeter funnel. The Hall flow rate (FR_H) is a corrected number reported in units of s/50 g, to the nearest second. The correction factor is based on the calibrated flow rate (40.2 s) of the flowmeter funnel [69].

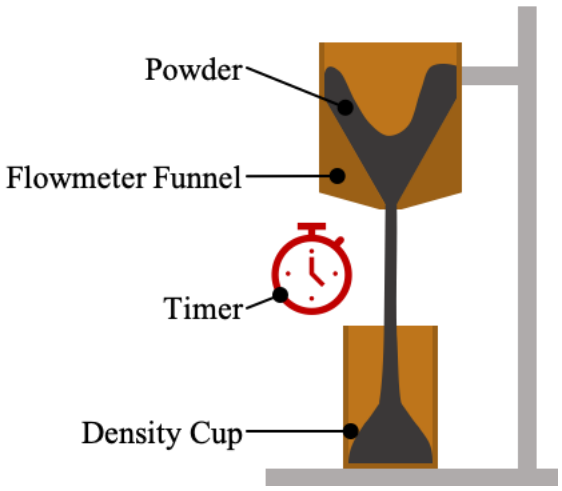

Figure 11. Schematic of a Hall Flowmeter funnel.

Powder Morphology **–** The powder morphology of the five different powder types were compared using scanning electron micrographs taken on a Zeiss Sigma 500 VP SEM at 100 X, 1,000 X, and 15,000 X. The powder was mounted to a microscope stub using double-sided carbon tape dipped into the powder container. Images were also taken of the SP313_C powder after being sieved using a 38 μm mesh.

3.2 Parameter Optimization

To determine optimal printing parameters for printing carbides, the investigation was broken into two separate experiments. This gave a clear picture of how the powder packing can be optimized without having the influence of printhead-specific parameters. The printer used was an ExOne X1-Lab printer, which uses a feed box and roller (Figure 9a) for powder deposition.

A series of preliminary tests were run at various parameters to narrow the values to a reasonable range that would provide consistently usable results. The values and powder used in the parameter optimizations were based on these tests.

3.2.1 Powder Bed DOE

The powder bed DOE focused on the optimization of spreading, allowing for the highest packing density within the entire powder bed. By optimizing this outcome, the resulting printed parts should have higher green densities due to the higher packing density of the print bed.

Three factors play a role in powder packing of the print bed: layer thickness, roller traverse speed, and the feed. For each of these factors a high (+) and low (-) value were chosen based on literature and previous results, creating two levels for each. The two levels and three factors create a 2^3 full factorial design. Table 3 gives the factors and levels that were used to create the experimental design. Kept constant in this DOE was the initial feed powder weight, the initial build depth, and the initial feed depth.

The DOE function, available in MiniTab software, was used to design and randomize the experiment using the parameter sets in Table 3. The experiment design, with 8 runs, is shown in Table 4.

Table 3. Values for the three factors that were tested with two levels for each factor.

Variables	Levels	
	-1	**+1**
Layer Thickness (μm)	50	100
Roller Traverse (mm/s)	5	15
Feed Ratio	1.5	2

Table 4. Experiment setup for the 2^3 full factorial design, generated using MiniTab.

Run	**Layer Thickness (μm)**	**Roller Traverse (mm/s)**	**Feed Ratio**
1	100	5	1.5
2	50	15	1.5
3	50	15	2
4	50	5	1.5
5	100	5	2
6	100	15	2
7	50	5	2
8	100	15	1.5

During printing, the printhead jets were disabled and the dry time was set to zero seconds so only powder was present in the powder bed. The build depth was 1.08 cm, which is similar to what is typically used while printing standard cubes. Each run was started with the same initial mass of 12.1 wt.% Co spray dried powder, provided by General Carbide, and sieved through a 38 μm mesh sieve. Only the three factors of interest were changed, based on the experiment setup in Table 4.

Powder Bed Packing Density – The powder bed packing density was calculated using the following equation:

$$\rho_{\text{packing}} = \frac{V_{\text{powder}}}{V_{\text{extracted powder}}}$$ **Equation 3**

where ρ_{packing} is the packing density, V_{powder} is the powder weight divided by the material density (14.29 g/cm^3, provided by General Carbide) and $V_{\text{extracted powder}}$ is the volume of the build box.

Many studies use the "plug method" for powder bed density measurements, where a sharp-edged punch tool of known diameter is used to extract a section of powder which is then weighed and divided by the volume of the plug [63, 70]. This method was not used in this study due to the stickiness of the powder and difficulty in spreading. It was thought that inserting a plug could cause too much compaction on the surrounding powder, causing the volume of powder captured to be inaccurate. Because the powder bed for the ExOne X-1 Lab printer is relatively small, the entire powder bed was taken into account for packing density measurements.

3.2.2 Print Parameter DOE

To further investigate the optimization of the printing parameters, a second design of experiments will be used. The second part will take into consideration binder saturation and dry time and how they influence the green density of the carbide parts. By using the optimal powder packing parameters to optimize the print factors, the resulting printed parts should have the highest green densities possible.

Two factors play a role in the binder distribution during printing: binder saturation and dry time. For each of these factors a high (+), medium (0), and low (-) value were chosen based on literature and previous results, creating three levels for each. The three levels and two factors create a 3^2 full factorial design. Table 5 gives the factors and levels used to create the experimental design.

Table 5. Values for the two factors that were tested with three levels for each factor.

Variables	Levels		
	-1	**0**	**+1**
Binder Saturation (%)	160	200	240
Dry Time (s)	30	45	60

Using the DOE function in MiniTab, the experiment design was created and randomized after specifying the desired parameters from Table 5. The full randomized experiment design consisting of nine runs is shown in Table 6.

Table 6. Experiment setup for the 3^2 full factorial design, generated using MiniTab.

Run	**Binder Sat. (%)**	**Dry Time (s)**
1	240	45
2	200	45
3	240	60
4	160	60
5	160	30
6	240	30
7	200	60
8	160	45
9	200	30

Binder Saturation **–** It is important to note that binder saturation is dependent on the powder packing rate, according to Equation 1. The default packing rate on the ExOne machines is set to 60%, meaning that 60% of the volume is occupied by solid powder. For a powder made up of granules such as WC-Co, the packing rate is much smaller due to the increased void spaces within the granules themselves. As a result, the input values of saturation of 160, 200, and 240% result in actual saturations of 80, 100, and 120%, respectively, based on measured powder packing rates.

Binder Jet Printing – Printing was done using a layer thickness of 100 μm, a feed ratio of 2, and a roller traverse speed of 5 m/s. 12- 10 mm x 8 mm x 5 mm rectangular prisms (Figure 12) were printed from the same 12.1 wt.% Co spray dried powder as used in the print bed DOE. The powder was sieved in a 38 μm sieve before each run. Prints were cured at 180 °C for 8 hours. Samples were taken out of the powder bed using tweezers and photographed. Linear dimensions for as many parts as possible were measures and six of the twelve samples were sent to General Carbide for sintering.

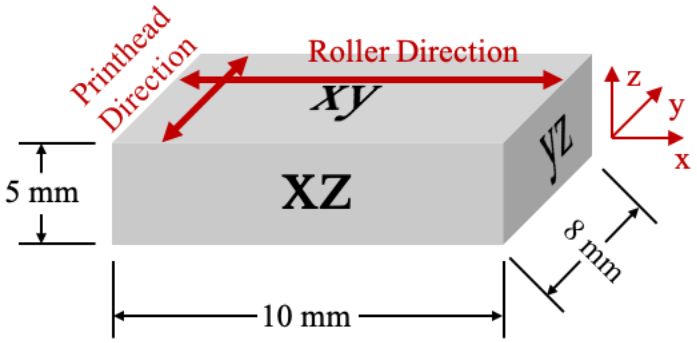

Figure 12. Printed coupon dimensions.

Green Density – Green density measurements were attempted on at least six parts for all runs. In some cases, the parts were too fragile, so fewer green densities were calculated due to broken parts. The green density calculation is done by taking the density of the part (mass/volume, determined using a balance and calipers) and dividing it by the theoretical density for a solid part of the same volume (using 14. 29 g/cm^3, provided by General Carbide for the corresponding powder lot). The dimensions were measured using calipers and the mass was measured using an Ohaus AX324 analytical balance to the nearest mg. The average green density for each run was reported for use in creating the main effects plot. The remaining six parts for each run were set aside for sintering.

Sintering **–** Samples were sintered at General Carbide in one of their standard sintering runs for pressed samples. Sintering was done at 1442 °C.

Archimedes Density Measurements **–** Once sintered samples were returned, Archimedes density measurements were performed to obtain the sintered density of the samples. The Archimedes method is used to determine the density of a sample by measuring the mass of the sample in air and in a fluid, such as water. From these two measurements, along with the density of the fluid, the density of the part can be calculated via the following equation:

$$\rho_{\mathrm{p}} = \frac{m_{\mathrm{a}}}{m_{\mathrm{wet}} - m_{\mathrm{fl}}} \cdot \rho_{\mathrm{fl}} \qquad \textbf{Equation 4}$$

where ρ_{p} is the part density, m_{a} is the mass in air, m_{wet} is the mass of the wet sample in air with the surface lightly dried, and m_{fl} is the mass in the fluid, and ρ_{fl} is the density of the fluid.

Shrinkage **–** The shrinkage is calculated based on sintered part dimensions along all three axes. The sintered dimension is compared to the green part dimension and a shrinkage value for each axis was calculated according to the following equations:

$$s_x = \frac{g_x - d_x}{g_x} \cdot 100 \qquad \textbf{Equation 5}$$

$$s_y = \frac{g_y - d_y}{g_y} \cdot 100 \qquad \textbf{Equation 6}$$

$$s_z = \frac{g_z - d_z}{g_z} \cdot 100 \qquad \textbf{Equation 7}$$

where *s* is the percent shrinkage, *g* is the green part dimension and *d* is the sintered part dimension.

Sample Preparation **–** From the six sintered samples for each run, three were cold mounted using Buehler EpoxyCure 2 Resin and Hardener. The three samples were mounted on the x-y, x-z, and y-z planes (Figure 12) for each of the nine runs, for a total of 27 mounted samples. The mounted samples were ground and polished using the following steps: 68 μm 8” Grind Abrase

Standard Diamond Wheel, 8” Omni-Brade Rough Polish Diamond Wheel, Broadcloth with Hyprez Five Star Diamond Compound using a Struers LaboPol-5 machine.

3.3 Characterization Methods

3.3.1 Mechanical Properties

Hardness **–** Vickers hardness measurements were performed on all 27 mounted samples with a 1 kgf and 10 s dwell time using a Rockwell Wilson 754 fitted with a custom Vickers tip. For the x-y, x-z, and y-z plane samples, 20, 15, and 12 indents were performed, respectively, according to the grid pattern in Figure 13.

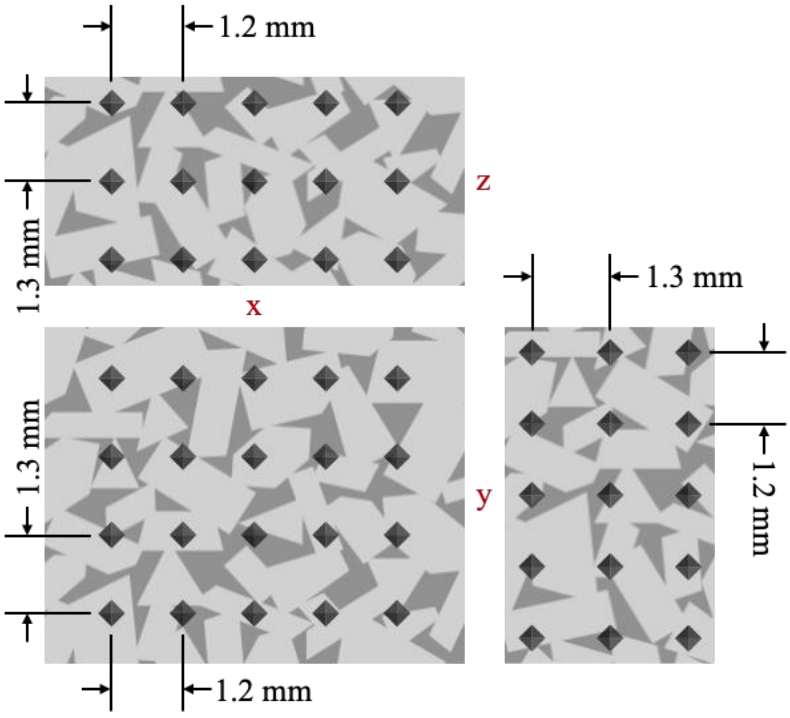

Figure 13. Layout of indents for hardness measurements.

Toughness **–** Toughness measurements were taken according to ISO 28079 using the Rockwell Wilson 754 machine with the custom Vickers tip at either a 30 or 100 kgf load. For all runs except Run 2, there was no cracking at 30 kgf, so a 100 kgf load was used. Cracks were observed using a Zeiss SmartZoom5 optical microscope and crack lengths were measured using ImageJ [72]. Three indents were made per sample. Palmqvist fracture toughness (W_K [$N/m^{3/2}$]]) was calculated using the following equations:

$$W_G = \frac{P}{T} \quad \textbf{Equation 8}$$

$$W_K = A \cdot \sqrt{H}\sqrt{W_G} \quad \textbf{Equation 9}$$

where W_G is the Palmqvist toughness [N/mm], P is the applied load [N], T is the total crack length [mm] (i.e. the sum of all four cracks), A is an empirical constant, and H is the hardness at the applied load [N/mm^2] [48, 49]. The constant A varies, depending on the model used. In this experiment, the model developed by Shetty will be used, with the corresponding constant of 0.0889, which has been demonstrated as the most accurate for WC-Co [48, 49].

3.3.2 Microstructural Analysis

Optical Microscopy (OM) **–** Images were taken of the top surface of the green samples for all printed samples using the Zeiss SmartZoom5 Optical Microscope at 100 X magnification. One sample from the low-, medium-, and high-density categories were selected for further imaging. Once samples were sintered, micrographs of all six faces were taken at 40 X for the three selected sintered samples. Stitched images were taken at 430 X of the mounted cross-sections of all sintered samples. Images of the green part surface were used to observe surface characteristics from printing and the sintered image surfaces were used to observe final part edge and corner retention,

potential cracking, and shrinkage. Finally, the stitched images of the mounted samples were used to observe Co pooling, porosity, and internal printing defects.

Scanning Electron Microscopy (SEM) – SEM micrographs were taken of the three low-, medium-, and high-density sintered samples using a Zeiss Sigma 500 VP SEM at 100 X, 500 X, 1000 X, 1500 X, 2000 X, 5000 X, and 10,000 X to observe the microstructure.

Stereology was performed on SEM images to determine grain sizes for the three selected samples using the line intercept method. A 10 x 10 grid was used with 4 μm line spacing.

Energy-Dispersive X-Ray Spectroscopy (EDS) – EDS area scans were completed using the ZEISS Sigma 500 VP SEM equipped with Oxford Aztec X-EDS at 5000 X magnification and a working distance of 8.5 mm with a 20 kV accelerating voltage to acquire compositional data for tungsten and cobalt.

Elemental Analysis – General Carbide performed LECO analysis of three samples to determine the carbon content. This information was combined with X-Ray Fluorescence (XRF) data (for W and Co content), provided by Clark Testing, to determine the final compositions of the three samples.

X-Ray Diffraction (XRD) – A Bruker AXS D8 Discover XRD was used to scan the xy mounted and polished cross-section for each run. Cu-Kα radiation was used over a 2θ range of 25º to 95º using a scan speed of 0.50 s/step and a 0.02º step size at room temperature.

3.3.3 Magnetic Properties

Vibrating Sample Magnetometer (VSM) – Room temperature hysteresis loops from -15 kOe to 15 kOe were measured using a LakeShore 8600 VSM. Magnetic saturation (M_s) and coercivity (H_c) were determined from the hysteresis curves for all runs.

4.0 Experimental Results

4.1 Powder Characterization

Flow Tests – The flow rate values from the Hall flow test are reported in Table 7. The three heat-treated powders did not flow. However, the standard powders and the heat-treated powder with a smaller size distribution all flowed. Interestingly, as the cobalt content increased, the flow rate increased for the non-heat-treated powders.

Table 7. Flow test results for spray dried powders.

Powder	**Mass (g)**	**Hall Flow (s/50 g)**
SP03_B	50.0	No flow
SP15_B	50.0	No flow
SP25_B	50.0	No flow
SP03_A	50.0	23.38
SP15_A	50.0	32.34
SP25_A	50.0	39.50
SP13_C	50.0	21.89

Powder Morphology – Micrographs of the powder are shown in Figure 14. It can be seen that the SP (spray dried) powders contain spherical granules and the GC (vacuum dried) powders do not. Additionally, the plasticizer can be seen surrounding the powder particles in the 15,000 X images of the GC15_A and SP15_A powders.

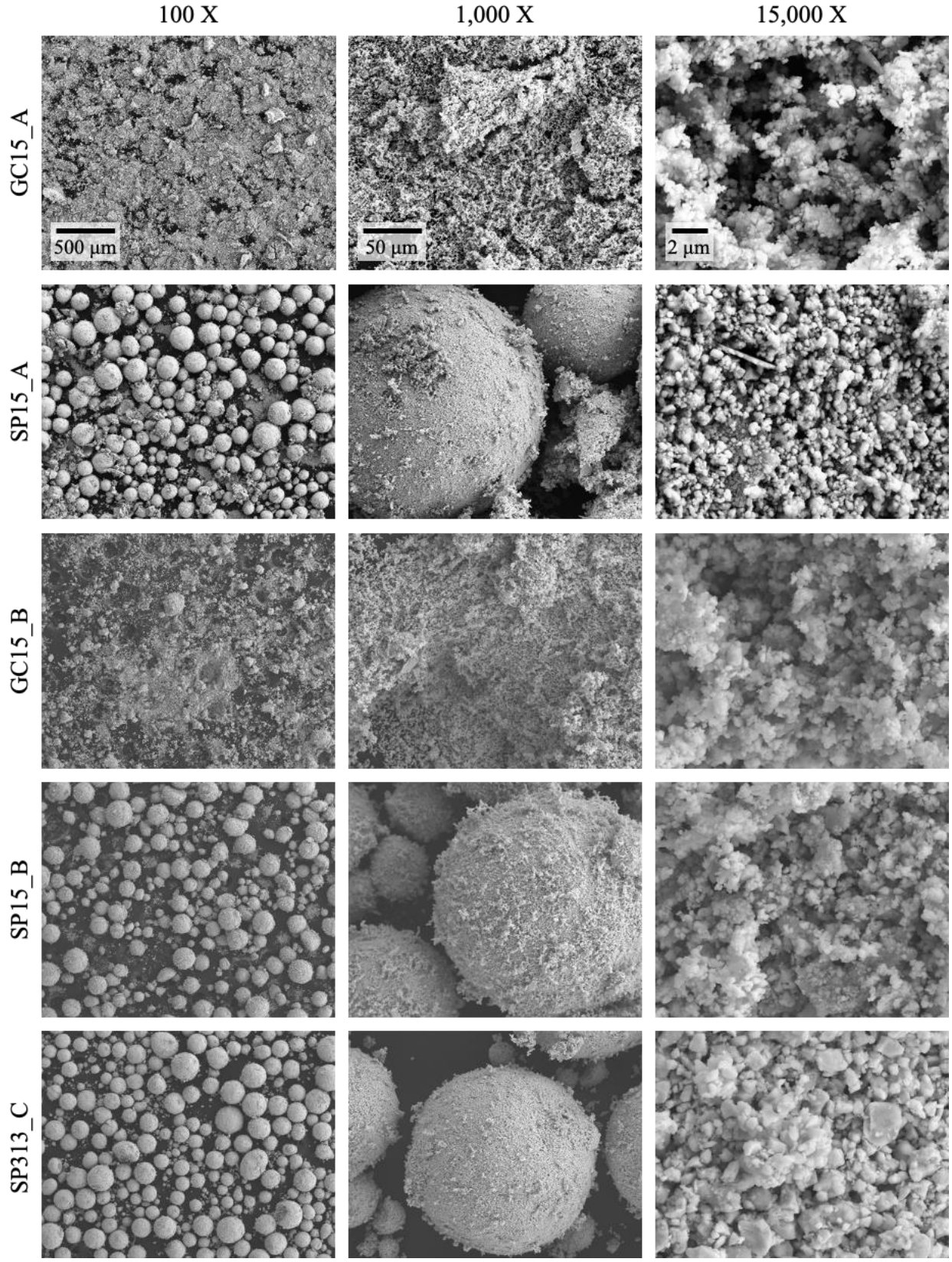

Figure 14. SEM micrographs of powders at various magnifications.

The SP313_C sieved powder sample images are presented in Figure 15. The morphology of the powder after sieving became more like that of the vacuum dried powder. Despite this change in morphology, after preliminary testing, the sieved powder resulted in the strongest parts with the highest green densities, so it was selected as the powder to use for the remainder of the experiment.

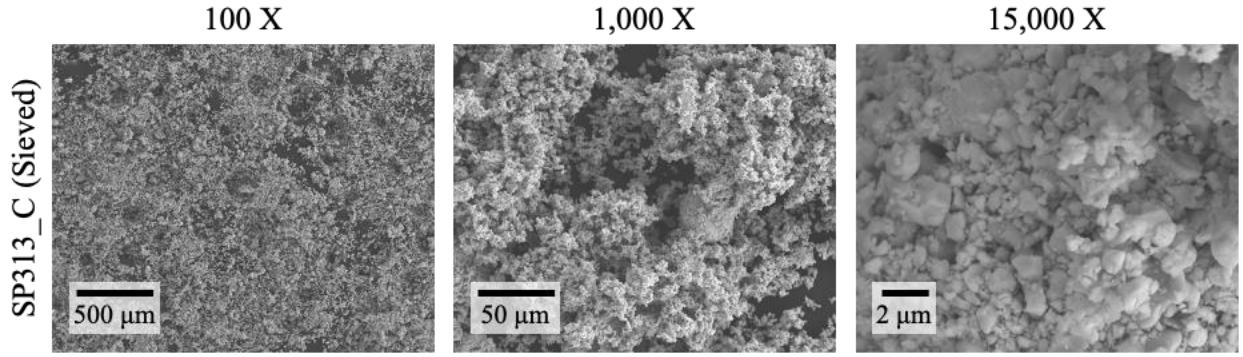

Figure 15. SP313_C Sieved powder micrographs.

4.2 Parameter Optimization

4.2.1 Powder Bed DOE

***Packing Density* –** Powder bed packing densities were measured for all 8 runs and values are presented in Table 8. It was noted during some runs that the powder bed did not fill completely, indicating that in some cases the parameter sets are inadequate for filling the layers sufficiently.

***Main Effects* –** The main effects plot for the powder bed DOE is presented in Figure 16. The layer thickness has the largest slope and the roller traverse hast the smallest slope, indicating that it influences the packing density much less than the layer thickness and feed ratio.

Table 8. Powder bed packing densities for powder bed DOE runs.

Run	Layer Thickness (µm)	Roller Traverse (m/s)	Feed Ratio	Packing Density (%)	Notes
4	50	5	1.5	21.00	Full
7	50	5	2	17.20	Left slide slopes down
2	50	15	1.5	19.56	Small section with divot - left side
3	50	15	2	17.47	Left side slopes down
1	100	5	1.5	20.41	Full
5	100	5	2	20.49	Full
8	100	15	1.5	19.35	Very small divot on left side
6	100	15	2	19.83	Full

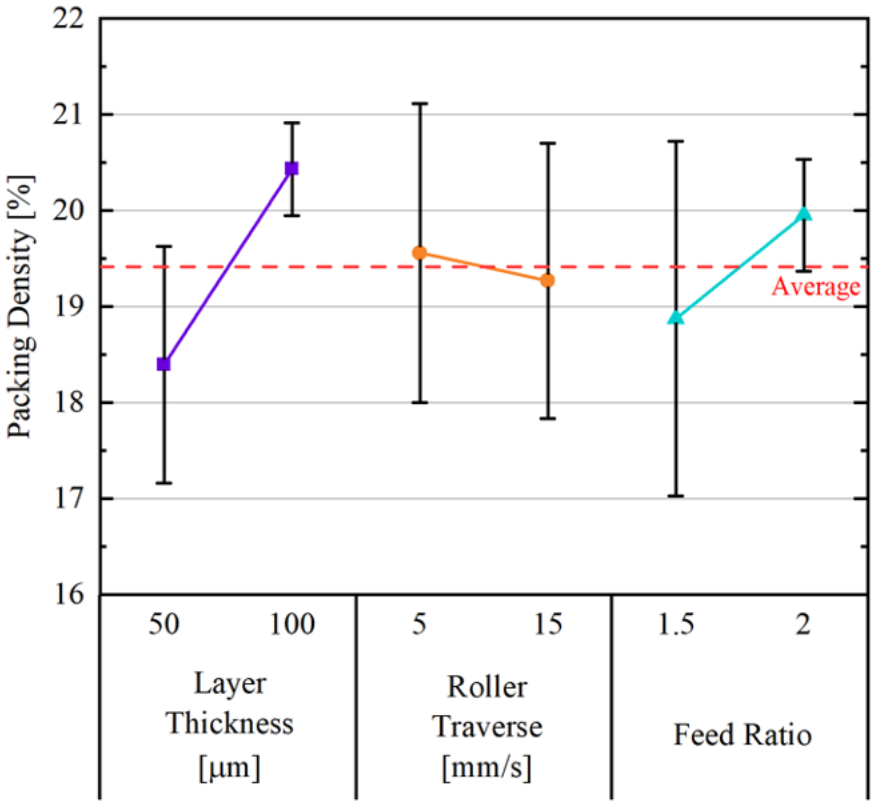

Figure 16. Main effects plot for the powder bed packing density DOE.

The influence of parameters can be verified in Table 9 where the layer thickness has the largest effect on powder bed packing density, followed by feed ratio, and finally roller traverse speed. The parameter effects were calculated using Equation 2. It is also interesting to note that the roller traverse is the only parameter that has a negative response associated with it; both the layer thickness and feed ratio show a positive response.

Table 9. Parameter effects for powder bed DOE.

Parameter	**Parameter Effect**
Layer Thickness	2.0
Roller Traverse	-0.3
Feed Ratio	1.1

The values that resulted in the highest green density for each parameter were selected for use in the final print parameter DOE.

4.2.2 Print Parameter DOE

***Green Density* –** The measured average green densities for each run are presented in Table 10. Three groupings of low-, medium-, and high-green densities were evident in the results. The lowest green density parts had parameter sets that were mismatched, meaning that the high saturations were paired with the low dry times, and vice versa. The visual results of this mismatch can be seen in Figure 23. The data is also visually represented in Figure 17 in terms of both binder saturation and dry time. There is no clear trend in the data.

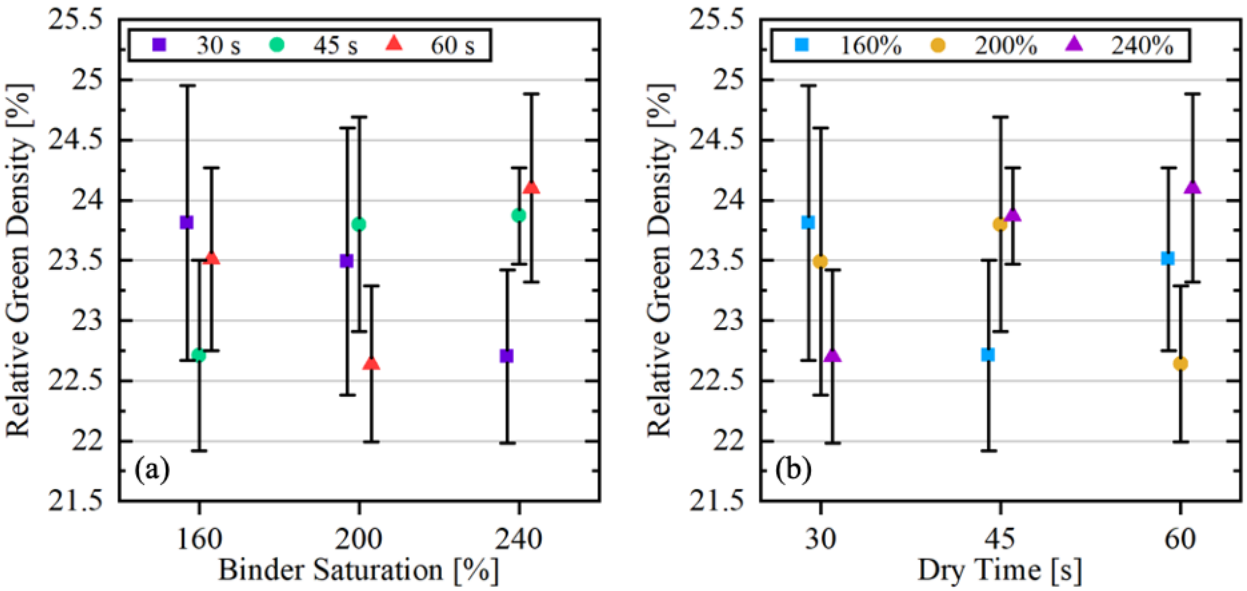

Figure 17. Green densities of samples in terms of (a) binder saturation and (b) dry time.

Table 10. Average green densities for each run, sorted from lowest to highest green density.

Run	Binder Saturation (%)	Dry Time (s)	Average Relative Density (%)
7	200	60	22.64
6	240	30	22.70
8	**160**	**45**	**22.71**
9	**200**	**30**	**23.49**
4	160	60	23.51
2	**200**	**45**	**23.8**
5	160	30	23.81
1	240	45	23.87
3	240	60	24.1

Sintered Density – Sintered densities, determined by Archimedes method, are shown in Table 11. Although slightly less clear, the same groupings can be made with the exception of runs

4 and 6. The highest relative bulk density achieved was 97.75% using a saturation of 200% and a dry time of 45 s.

Table 11. Average sintered bulk densities for all runs, sorted from highest to lowest density.

Run	Binder Saturation (%)	Dry Time (s)	Average Relative Density (%)
8	**160**	**45**	**93.97**
4	160	60	95.06
7	200	60	95.25
6	240	30	96.22
9	**200**	**30**	**96.47**
1	240	45	96.54
3	240	60	96.71
5	160	30	97.10
2	**200**	**45**	**97.75**

The same visual representation of the sintered density data is shown in Figure 18. In this case, a clearer trend can be seen for the high and low dry times. When the dry time is low, the bulk density decreases as saturation increases. On the other hand, when the dry time is high, the bulk density increases with saturation. For the case of the middle dry time, it increases and then decreases with increasing saturation.

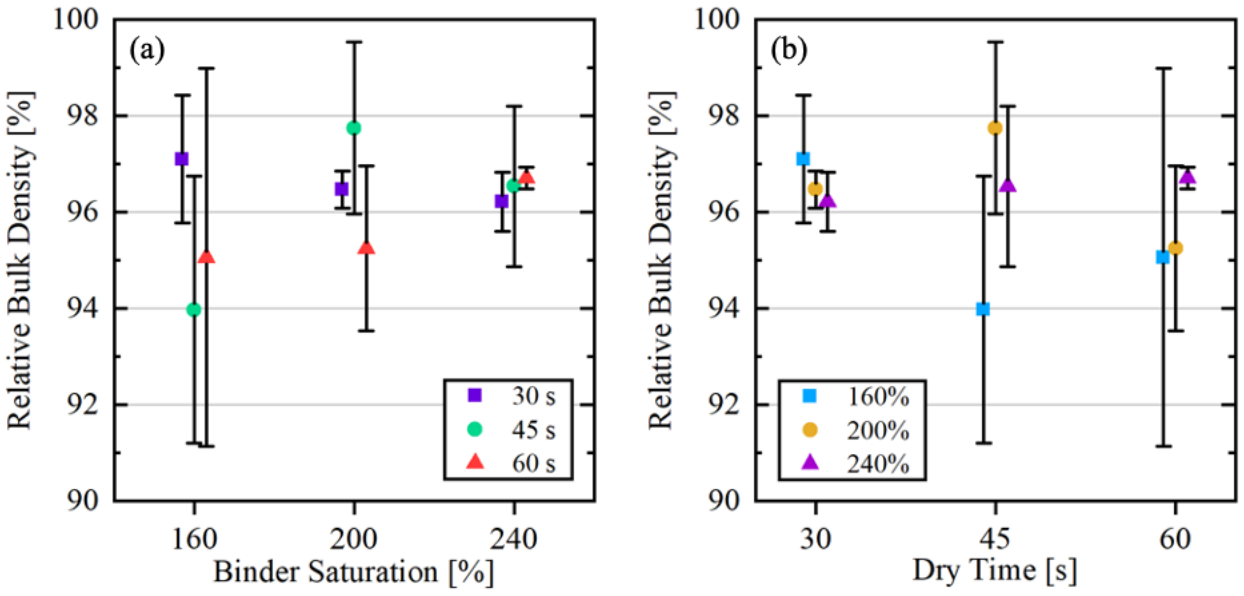

Figure 18. Average bulk densities in terms of (a) binder saturation and (b) dry time for all nine runs.

Shrinkage – The calculated average shrinkages for each run, in each of the three dimensions, are presented in Table 12 with a visual representation of the data shown in Figure 19.

Table 12. Average shrinkage in the x-, y-, and z- directions, sorted from highest to lowest.

Run	x [%]	*Run*	y [%]	*Run*	z [%]
5	37.77	*7*	36.49	*7*	41.13
4	37.58	*4*	36.45	*8*	40.96
2	37.24	*6*	35.99	*9*	40.55
8	36.95	*5*	35.22	*1*	40.20
6	36.93	*9*	35.17	*6*	38.85
3	36.73	*8*	35.11	*3*	38.68
7	36.71	*3*	34.88	*2*	37.36
9	36.52	*2*	34.82	*5*	37.25
1	36.32	*1*	34.81	*4*	35.55

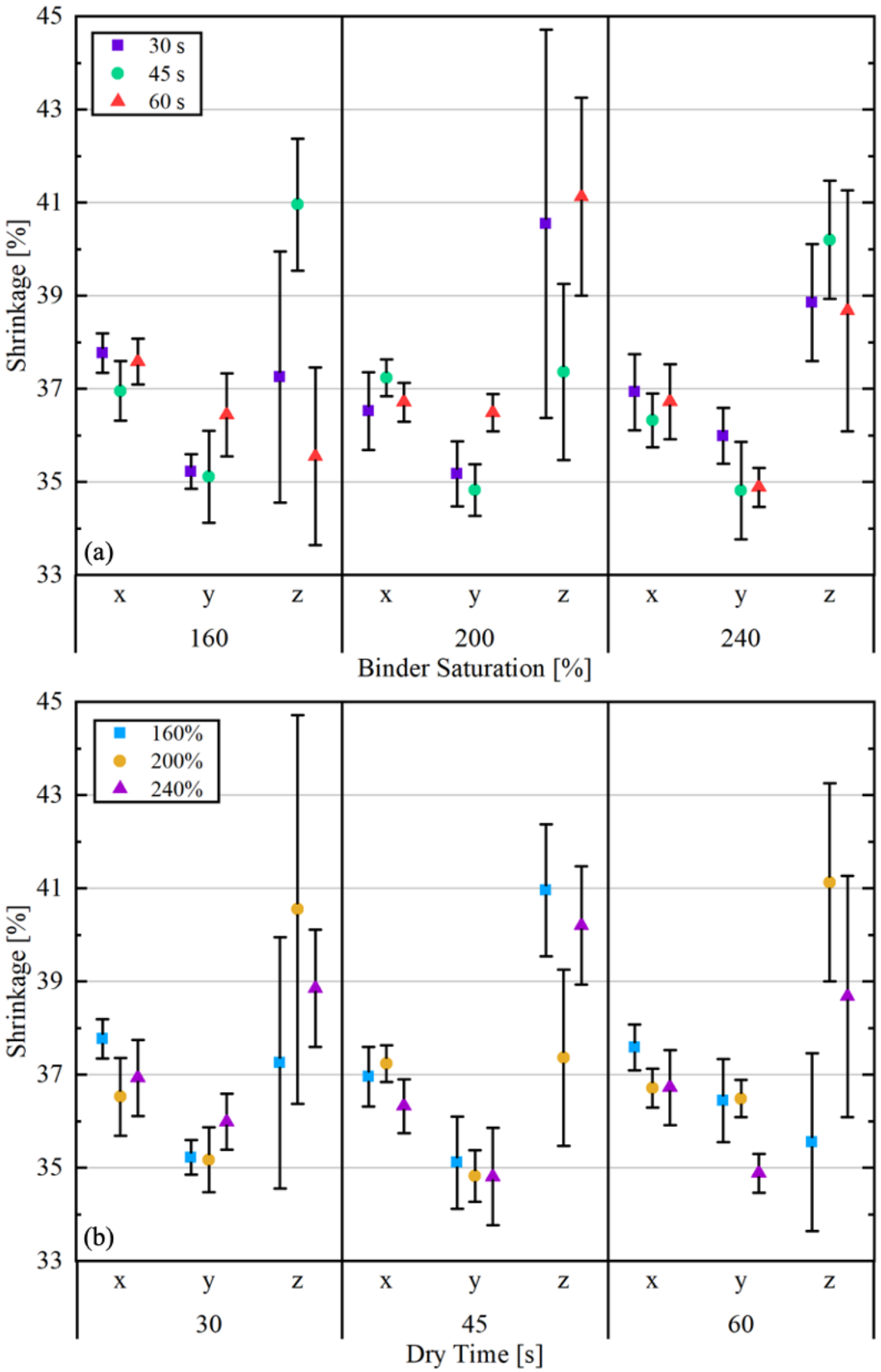

Figure 19. Average shrinkage in the x-, y-, and z-directions in terms of (a) binder saturation and (b) dry time.

Main Effects **–** The main effects plot for the print parameter DOE is shown in Figure 20. It can be seen from the figure that there was not a large effect of either parameter. It is also important to note the high standard deviations present in this study.

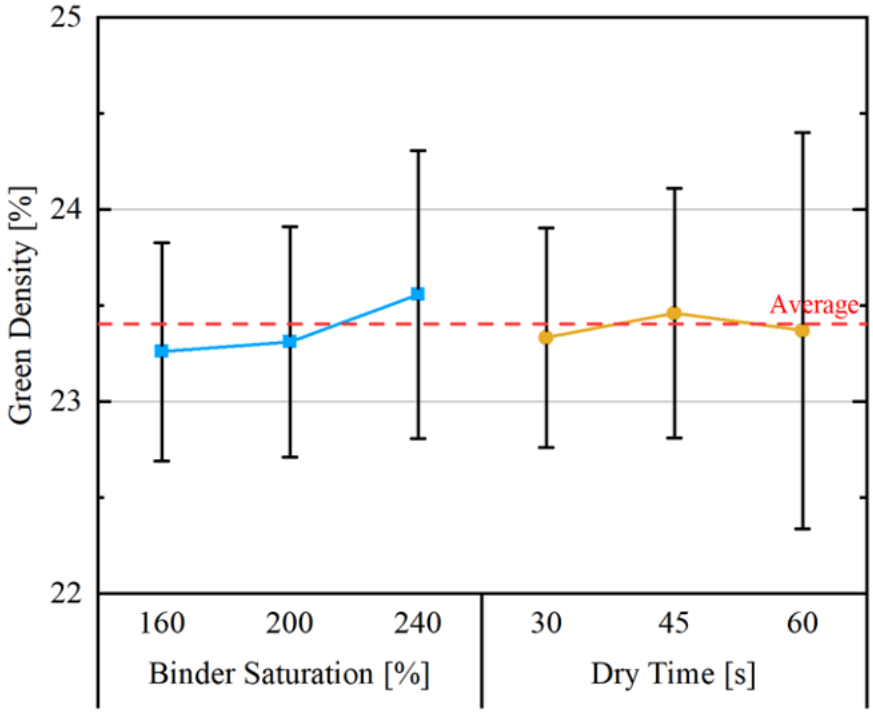

Figure 20. Main effects plot for dry time and binder saturation.

The parameter effects of binder saturation and dry time are reported in Table 13. The effects were calculated from the high and low values of each parameter set. The binder saturation had a larger effect on green density than dry time did.

Table 13. Parameter effects for binder saturation and dry time.

Parameter	**Parameter Effect**
Binder Saturation	0.30
Dry Time	0.04

4.3 Characterization

4.3.1 Mechanical Properties

Hardness **–** The results from Vickers hardness tests are shown in Figure 21. The overall spread of hardness values appears to be higher for the larger saturations but due to the high standard deviations, it is difficult to make a confident claim. The hardness increases with increasing saturation for 45 s dry time runs.

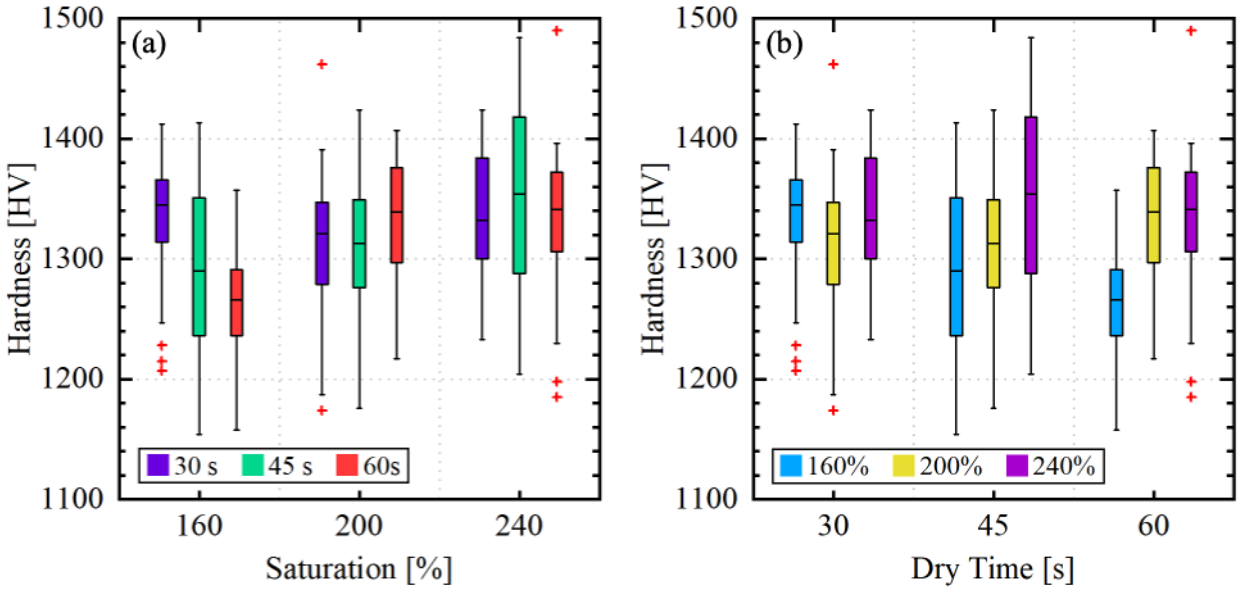

Figure 21. Vickers hardness results in terms of (a) saturation, and (b) dry time.

Toughness **–** Fracture toughness measurements are shown in Figure 22. A couple similar trends are seen when compared to hardness, but overall, trends are difficult to confirm due to the high standard deviations.

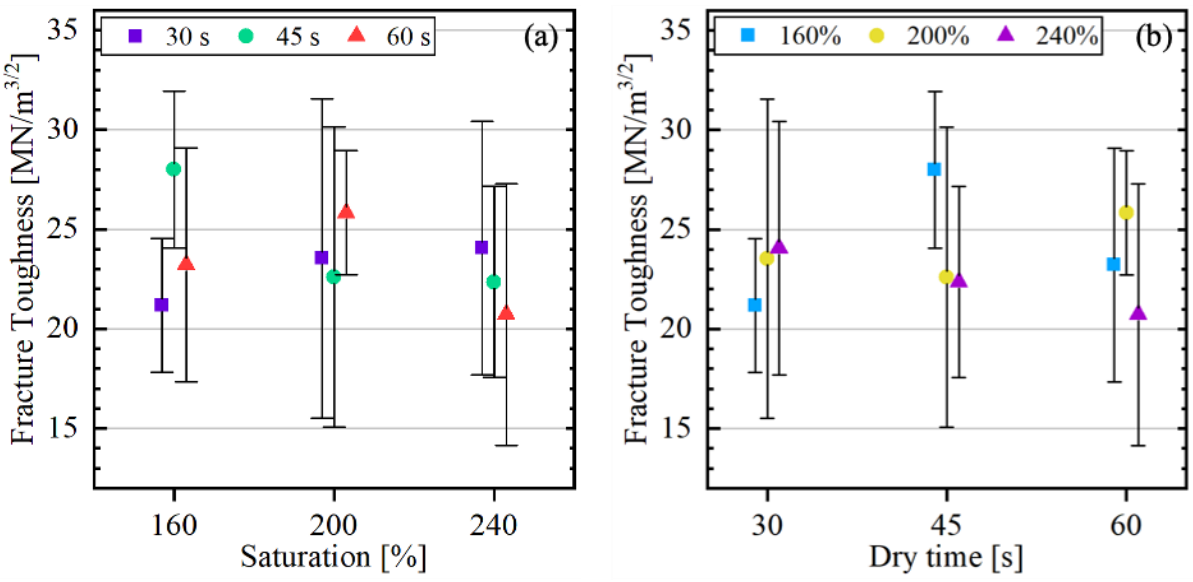

Figure 22. Fracture toughness results in terms of (a) saturation and (b) dry time.

4.3.2 Microstructural Analysis

The low-, medium-, and high-density samples selected for SEM and EDS measurements were from runs 8, 9, and 2, respectively. The selections were based on according to sorted green and sintered densities (Table 10 and Table 11) were chosen to further analyze via SEM and EDS.

Optical Microscopy **–** Micrographs of the top surfaces of the green samples are shown in Figure 23. Lines can be seen on the surface from binder jetting and agglomerated of powder can also be seen in the samples printed with higher saturation. High dry times and low saturation show a drier surface and samples printed with a higher saturation and lower dry time have more powder agglomerates that form on the surface.

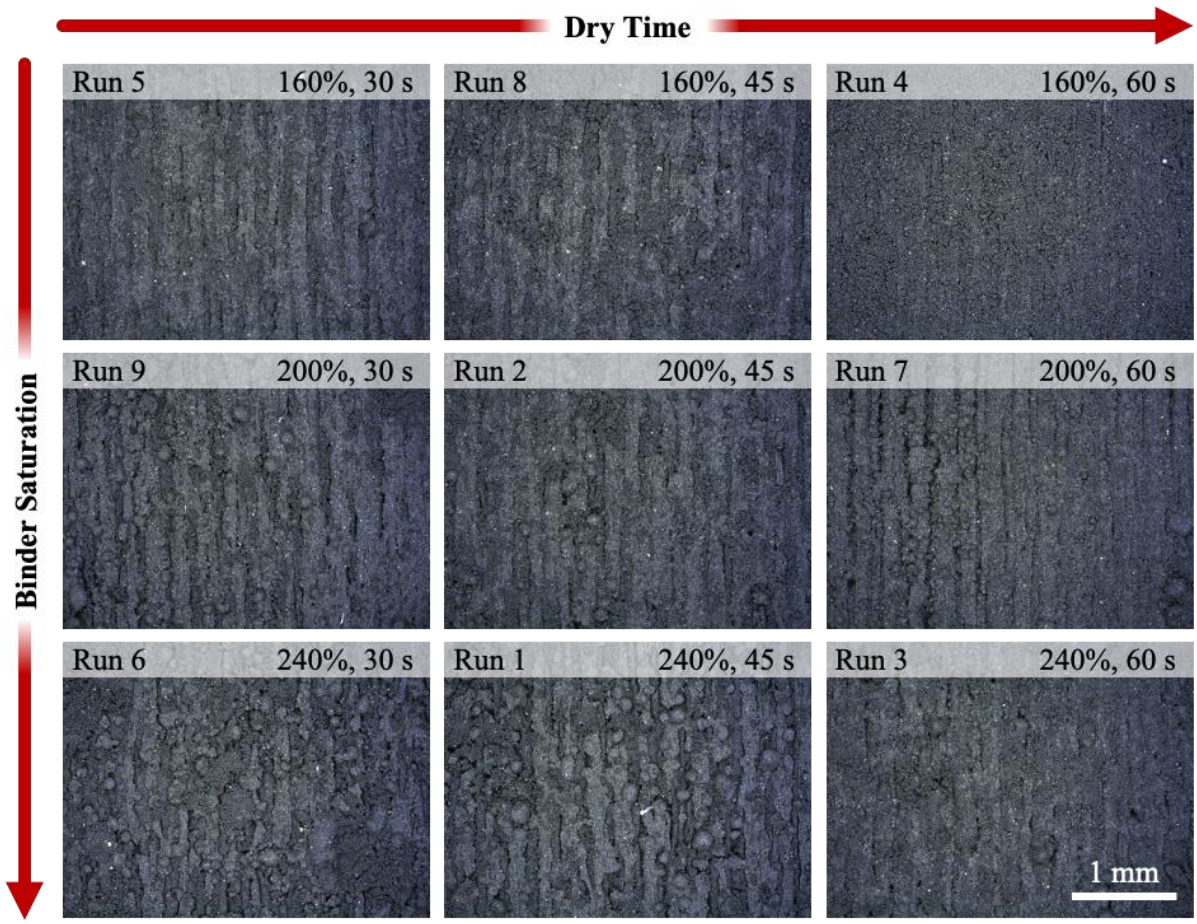

Figure 23. Green surfaces from a sample of each run, sorted by increasing saturation and dry time.

After sintering, optical micrographs of the six surfaces were taken for the selected low-, medium-, and high-density samples (Figure 24). Discoloration is due to oxidation that formed on the surface after being submerged in water for Archimedes density measurements. Cracking and surface porosity can be seen as well as layer delamination, especially along edges. Other surface defects are a result of green part handling.

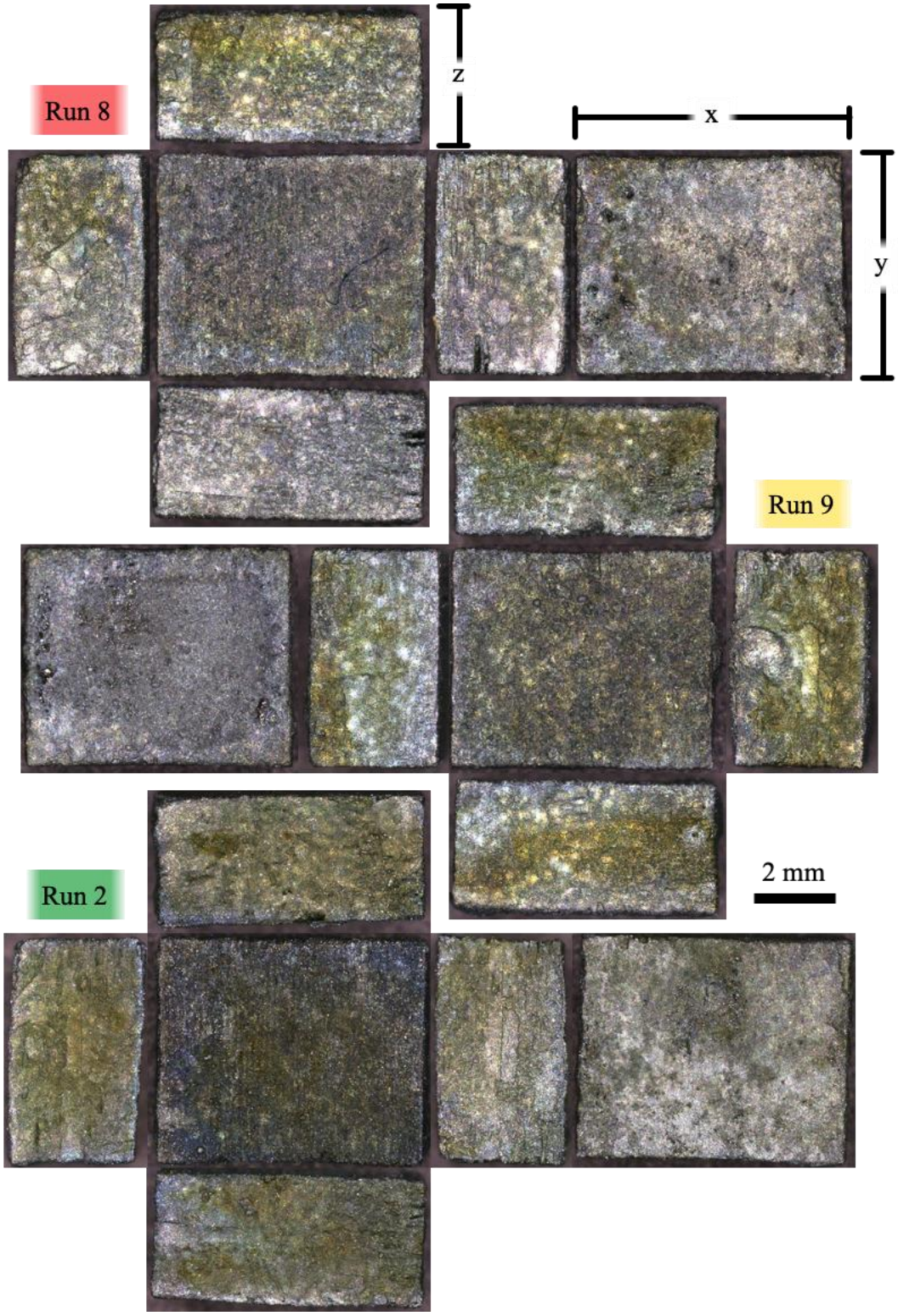

Figure 24. Sintered surfaces of a sample from runs 8, 9, and 2.

Cracking, surface roughness, and porosity (black spots), and Co pooling (dark areas) can be seen in the stitched optical micrographs that were taken of the xy, xz, and yz mounted cross-sections, as shown in Figure 25.

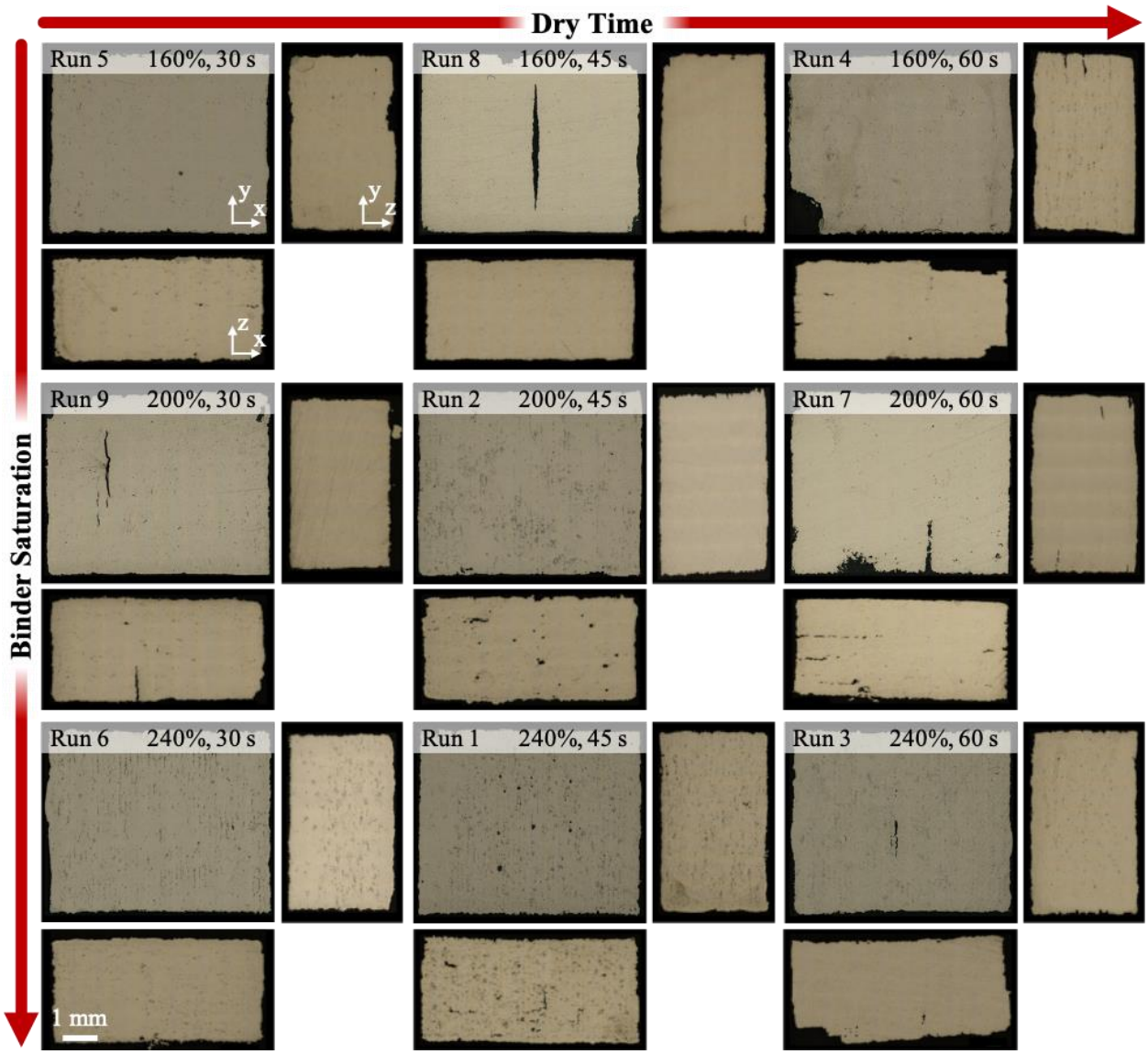

Figure 25. Stitched overview optical micrograph of xy, xz, and yz cross-sections for one sample per run.

Scanning Electron Microscopy – Images showing the microstructure for the low-, medium-, and high-density samples are shown in Figure 26. Cobalt pooling, evidenced by the dark regions between WC grains, can be seen in all samples. Grain sizes are reported in Table 14.

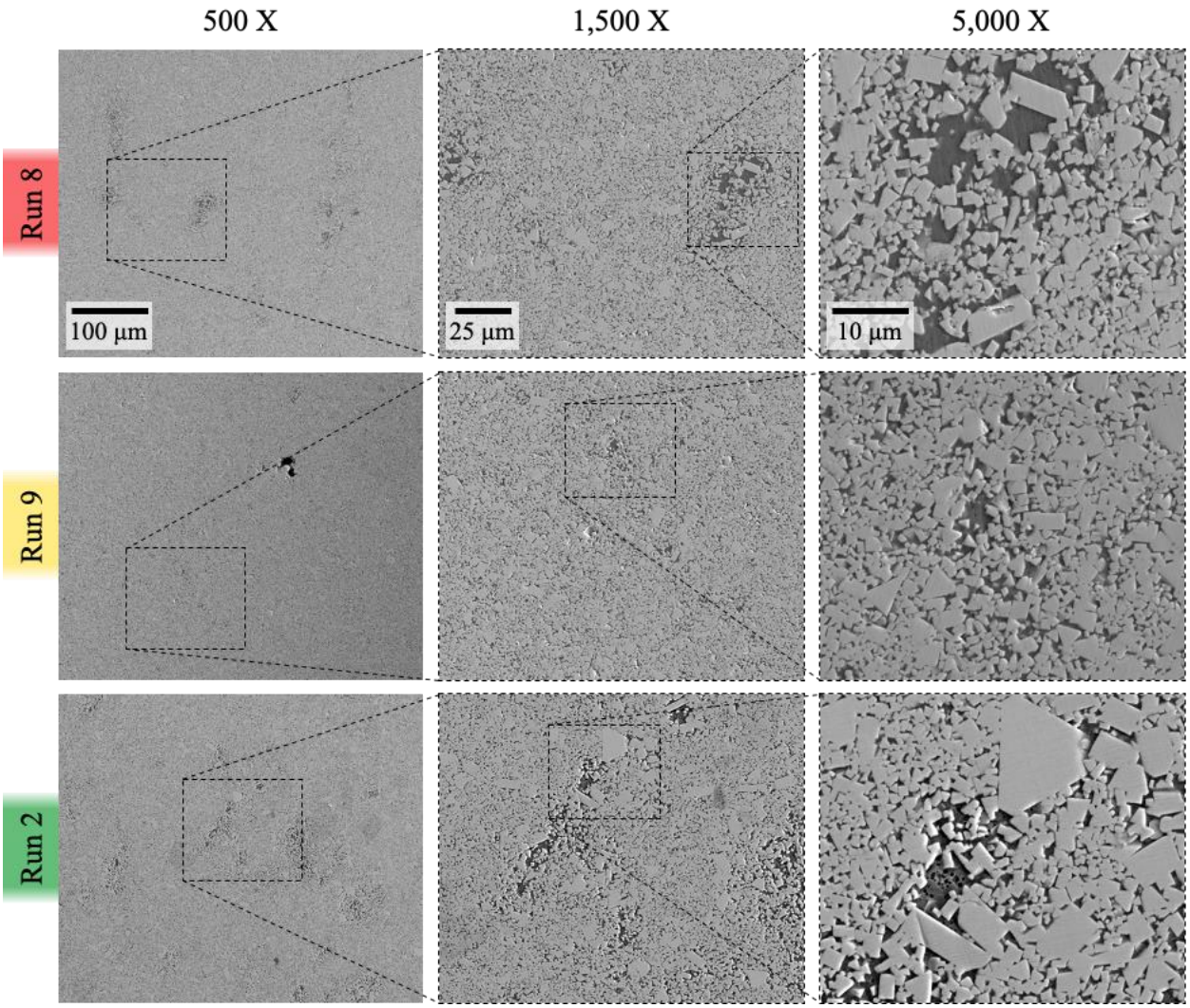

Figure 26. SEM micrographs at various magnifications for the low-, medium-, and high-density samples.

Table 14. Average grain sizes for selected runs.

Run	Average Grain Size [µm]
8	2.36
9	2.44
2	2.63

Elemental Analysis – Combined LECO and XRF results are reported in Table 15. The cobalt content was the closest to the powder composition (12.1 wt.%) for Run 8. The cobalt content was observed to increase for Runs 9 and 8. Additionally, the W/C atomic ratio is very close to 1:1 for all three samples.

Table 15. Elemental analysis results for Run 8, 9, and 2 from combined LECO and XRF data including the atomic ratio of W/C.

Run	**W/C**	***Element***	**wt.%**
8	1.007	*C*	5.37
		Co	11.83
9	1.035	*C*	5.26
		Co	11.38
2	1.029	*C*	5.35
		Co	10.29

X-Ray Diffraction – The XRD scans are shown in Figure 27 for all nine runs. Based on peak analysis, there is no conclusive evidence of eta-phase in any samples. Reference patterns for five Co phases and three $(W,Co)_6C$ phases were compared to the XRD pattern with no peaks aligning with the small peaks.

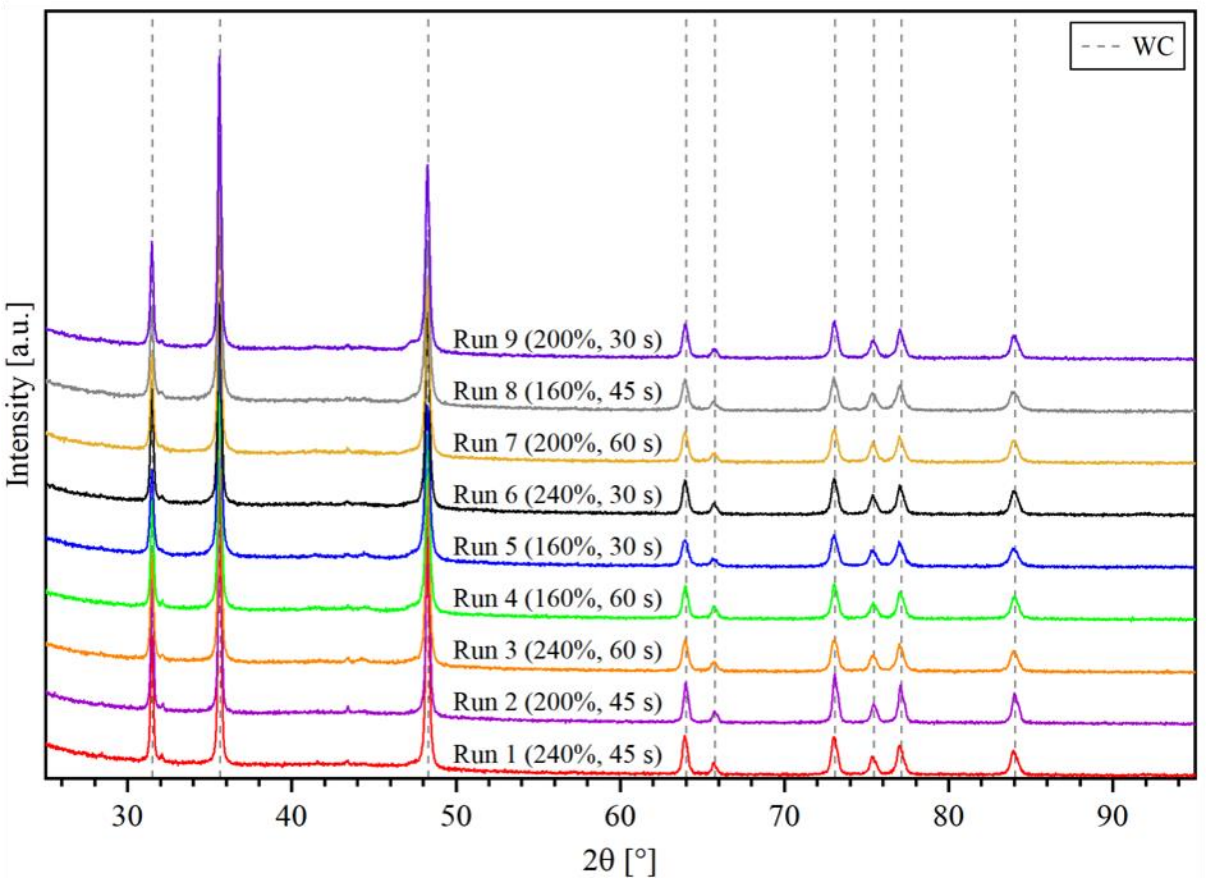

Figure 27. XRD Results for all runs with relevant peaks identified. Small unidentified peaks did not match any Co or $(W,Co)_6C$ reference patterns.

4.3.3 Magnetic Properties

***Vibrating Sample Magnetometer* –** Hysteresis curves are shown in Figure 28 for all nine samples. All samples showed a similarly shaped hysteresis curve.

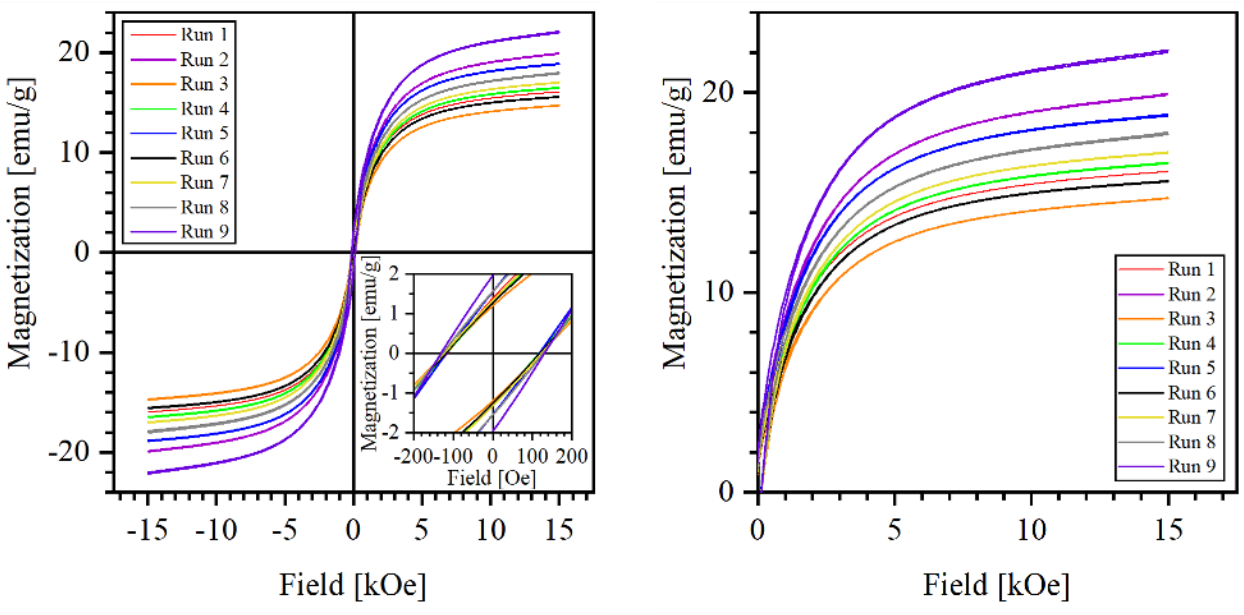

Figure 28. Magnetic hysteresis loops for all runs with inset showing detail at origin.

Saturation magnetizations between 14.7 and 22.1 emu/g and coercivities between 121 and 135 Oe were observed (Table 16), with the highest coercivity in run 2 and the lowest in run 5.

Table 16. Magnetic property values for all runs.

Run	**Binder Sat. [%]**	**Dry Time [s]**	**M_S [emu/g]**	**H_C [Oe]**
1	240	45	15.9	122
2	200	45	19.9	135
3	240	60	14.7	122
4	160	60	16.5	122
5	160	30	18.9	121
6	240	30	15.6	122
7	200	60	17.0	122
8	160	45	18.0	127
9	200	30	22.1	122

5.0 Discussion

Powder **–** Powder morphology was granules comprised of much smaller nanoparticles, revealed by SEM. The vacuum dried powder had much fewer granules whereas the spray dried powder was primarily granules. The powder morphology plays a large role in the flowability of the powder. Hall flow measurements revealed that the vacuum dried powder did not flow at all, a result of the lack of spherical morphology. On the other hand, the spherical granules in the spray dried powder aided in the flow of the powder. Interestingly, the heat-treated spray dried powder also did not flow. Despite maintaining the spherical morphology, the main difference in the heat treated versus non-heat-treated powder is that the non-heat-treated powder contains a plasticizer. The plasticizer therefore aids in the flow of the powder and without it, causes more sticking. Amongst the powders that did flow, the higher the cobalt content, the higher the flow rate. Powder flow rate is affected by the type of material. The difference in theoretical density between the three powders of different cobalt content could cause the flow rates to differ where materials with a high specific density have a high flow rate and vice versa [73]. As a result, since a higher cobalt content is present in the SP25_A powder it has a higher theoretical density, and it stands to reason that it has the highest flow rate of the spray dried powders.

Powder Spreading Parameter Optimization **–** The powder bed DOE provided important information for packing density of the powder. The packing density of the powder bed was less than the tap densities measured by General Carbide. This is expected due to the agglomerated nature of the WC-Co powder. The tap density measurement uses a slight tapping to allow the powder to settle which is not the case with the powder deposition method of BJ3DP. The roller does not impart enough force to bring the packing density of the powder to its standard measure.

Based on the results of this test, it can be concluded that the lower roller traverse speed helps the packing density to increase slightly. A low roller traverse speed allows a longer period of contact between the roller and the powder, forcing the powder to settle more than fast roller traverse speeds where the roller is in contact with the powder for a shorter period of time. Additionally, a higher feed ratio results in a higher powder packing rate. When more powder is available to be packed into the powder bed by the roller, the powder shifts and granules break up, allowing for an increase in packing density.

Although the roller traverse speed and feed ratio both have a minor effect on increasing packing density, the parameter with the largest effect on packing density was found to be the layer thickness. A layer thickness of 100 μm yielded the higher green densities. It is known that powder packing density is a factor of the layer thickness used. The counter-rolling layering, present in the X1-Lab and ExOne Innovent machines is not the most defect-avoiding spreading method and is generally appropriate for layer thicknesses >55 μm [5]. Therefore, a larger number of defects were likely present in the powder beds printed with a 50 μm layer thickness. The defects can include cavities and part shifting [5]. As a result, the powder beds printed with a layer thickness of 100 μm showed higher green densities.

The main effects plot (Figure 18) sums up the aforementioned results visually. It can be seen that the combination of a layer thickness of 100 μm, a roller traverse speed of 5 mm/s, and feed ratio of 2 is the optimal combination of spreading parameters for achieving high powder packing fractions in the powder bed. By optimizing the powder spreading for a high packing density, the printed samples will have superior green densities to samples printed without optimized spreading parameters. Even with the most optimal parameters, the packing rate of the

powder in the print bed was still about 5% less than the tap density of the powder from General Carbide, which was 25%.

Print Parameter Optimization **–** Optimization on the printing parameters focused on binder saturation and dry time. Binder saturation actually depends on the powder packing fraction [5]. Therefore, it was important to keep the powder spreading parameters constant when testing the effects of binder saturation on the green density of the WC-Co printed parts. The value for the packing fraction is not exclusively a result of the powder spreading parameters. The agglomerated property of the WC-Co powder causes the packing fraction to be much lower than traditional powder of the same size distribution. This causes some difficulty in the additive manufacturing process because the powder needs more binder to saturate the layers. Additionally, an overall lower green density occurs because of the excess void spaces, which leads, in general to a lower sintered density. The low green density values were seen in all samples of the print parameter DOE with the highest relative green density of ~24% (Run 3) and highest sintered density of ~98% (Run 2). As reported, the green and sintered densities fell into low, medium, and high categories of density, and were relatively consistent in category before and after sintering. It was observed that the samples printed with more well-matched dry times and saturations, i.e., a high value of saturation and a high dry time, a medium value of saturation and a medium dry time, and a low value of saturation and low dry time, all had higher green and sintered densities (Figure 17). This is in contrast to the samples printed with low dry times matched with high saturations and vice versa. The large standard deviations in green and sintered densities for the nine runs made it difficult to identify any clear trend in the data besides this.

Enneti, et al. has also conducted studies on the BJ3DP of WC-Co and has reported sintered density values between 92 and 94%. Additionally, shrinkages were reported between 22.2 and

24.1% along the x- and y-directions and between 23.1 and 24.4% in the z-direction. Eight out of 9 runs in this study produced results higher than the sintered densities reported by Enneti, et al. The shrinkages were around 15% higher in this study, pointing to a lower green density than achieved by Enneti, et al. [9]. Achieving higher sintered densities with heat-treated powder is a significant result. The powder used by Enneti, et al. was pre-sintered, meaning that the granules themselves were partially sintered. The resulting morphology is spherical, like the granules of this study, but in contrast to this study, pre-sintered powder cannot be broken apart into its smaller primary particles. As a result, the pre-sintered powder flows more like spherical metal powders. The use of sintered powder in BJ3DP is not available for study due to patent laws. As a result, achieving high sintered densities without the use of pre-sintered powder opens up many possibilities for smaller WC-Co manufacturers, such as General Carbide. There is a possibility of achieving even higher sintered densities by using pre-sintered powder in combination with optimized parameters.

In general, it is important that saturations and dry times are well-matched. Dry times that are too short result in dimensional inaccuracies and decreased strength due to excessive binder penetration in the vertical direction. On the other hand, dry times that are too high can result in delamination and poor strength due to the lack of a continuous liquid phase across the powder surface and a subsequent loss of inter-layer strength. The low specific density of binder, compared to that of WC-Co, means that the addition of more binder has negligible influence on the overall green density. Therefore, the difference in density among the various parameter sets can be attributed to the specific combination of dry time and saturation. Based on the effects of dry time previously mentioned, interlayer defects occur in the cases where dry time is too high, thus causing a lower green and sintered density. Evidence of these interlayer defects can be found in the xz- and yz-SEM cross-sections (Figure 25) of Run 4 and 7. These two runs had high dry time and

lower saturations, resulting in inter-layer delamination and cracking between layers from the surface. None of the other samples displayed this degree of inter-layer cracking. The cracking is the primary contributor to low green and sintered densities. The low dry times, on the other hand, caused excessive binder penetration and resulting low green and sintered densities due to the disturbance of the layer surface, resulting in poor spreading and increased porosity. The evidence of this surface disturbance for low dry times can be seen in Figure 23. It is evident that the layer surface for low dry time/high saturation combinations, linked to Runs 6 and 9, also with low green and sintered densities, is very rough and powder granules appear on the layer surface.

The powder-binder interactions on the layer surface during jetting is a topic that is being investigated more rigorously. For fine powders, as the binder drop penetrates the loose powder surface, spherical agglomerates form from the surrounding granules. This occurs because the binder is unable to penetrate the granules completely and pulls in the surrounding loose powder instead [5]. In cases where the space between primary particles is very small, the capillary forces of the voids does not exceed the surface tension of the liquid, and granules are unable to be fully penetrated by the binder, resulting in the formation of large granules on the surface of the layer, ultimately contributing to reduced powder spreading efficiency and lower green densities.

No trend was observed from the shrinkage data except that the largest shrinkages, and largest standard deviations, occurred in the z-direction. This is a common occurrence for BJ3DP parts because gravity plays a role in the vertical shrinkage. The presence of excess void spaces within the powder attributes to higher porosity, and lower green density, within the part. In traditional PM processes, the powder is pressed into a compact green part but he BJ3DP process uses no pressure, so the shrinkage is larger than traditionally manufactured WC-Co parts.

Based on the main effects plot and parameter effect calculation, the binder saturation had a larger effect on green density. However, the certainty of this claim is questionable due to the high standard deviations of the green densities for each parameter. As previously discussed, the dry time and saturation are dependent on each other. Therefore, it cannot be concluded which has a greater effect on green and sintered densities. Based on the sintered densities, the optimal printing parameters are as follows: binder saturation of 200%, dry time of 45 s.

The overall appearance of the sintered parts was very rough. The surfaces had cracking, imperfections, and visible print jet lines. The samples with higher green and sintered densities did show better surface finishes though (Figure 24). The high surface roughness is not ideal for wear parts such as WC-Co because the various rough spots provide areas of high stress concentrations which are initiation sites for crack formation. As a result, these parts would need to be machined in order to smooth the surface to a more reliable finish. Additionally, internal cracking and porosity, as seen in the black areas of Figure 25 are detrimental to wear part performance for the same reasons. By increasing the sintered density of these parts, internal cracks and porosity can be eliminated and crack imitation sites reduced. It is difficult to pinpoint a trend in the cracking and porosity of these parts due to the low precision of the results in this study. More work will need to be done to achieve more consistent results.

Material Properties – According to metrics provided by General Carbide, the fracture toughness of an acceptable 12.1 wt.% Co WC-Co alloy should fall between 9-15 $MPam^{1/2}$, depending on the grain size. Medium to coarse grained carbide should have a toughness of approximately 12-15 $MPam^{1/2}$ [74]. The values obtained in this experiment fell well above the acceptable ranges for toughness. Hardness, on the other hand, fell within the ranges for acceptable

industrial use (~1165-1430 HV) but had a much larger standard deviation with some values falling outside of this range.

The microstructure of the BJ3DP parts was not ideal for high-performing WC-Co. Frequent Co pooling was observed as dark regions between geometric WC grains (Figure 26), especially along layer (xz, yz cross-sections) and printhead (xy cross-sections) boundaries (Figure 25). Co pooling, in this case, is a result of the low density of the green parts. As liquid phase sintering proceeds, the Co liquid wets the WC grains. However, in the case of a low green density BJ3DP part, there is a significant amount of void space within granules and between layers. The Co would naturally pool in these areas due to the reduction of surface energy in a larger void. This results in Co pooling seen not only throughout the sample, but specifically in the areas where more voids were present, i.e., between layers and between jet paths.

The grain sizes observed in this study are consistent with medium- to coarse-grained WC-Co [1]. For a WC-Co part with 12.1 wt.% Co and medium grain sizes, the average hardness values achieved in this study fall in line with industry standards [74]. However, with the large standard deviations, hardness values also fall outside the range of the typical hardness values for this composition of WC-Co. The samples in the low range of hardness correspond to the higher toughness values, since there is a trade-off between hardness and toughness. The lower hardness achieved in these parts can be attributed to the significant Co pooling throughout the sample. On the other hand, samples that exhibit higher hardness and lower toughness could be a result of areas of the microstructure where the grain size is larger than average. Based on the micrographs, there are some regions that have excessive grain growth, leading to a higher hardness than the bulk of the sample. Further grain refinement is required to obtain a microstructure with consistent grain

sizes and less Co pooling to be able to consistently produce parts with both accurate and precise hardness and toughness values.

Compositionally, cobalt content decreases with decreasing sintered density. The cobalt percentage is lower than expected and can be attributed to possible eta phase formation. In examining the XRD patterns, it is not evident that any eta phase peaks occur. However, cobalt, which is definitely in the parts, does not appear either. Therefore, since eta would exist to a much smaller extent than cobalt, a conclusion cannot be drawn on the presence of eta phase due to the low intensity XRD peaks of cobalt. Optical micrographs of etched samples do not clearly show the eta phase either, as it is possible to be mistake finely dispersed eta phase for porosity in samples that are not fully dense. Further, the carbon contents for all three samples (Run 2, 8, 9) fall within very close proximity to the phase boundary between WC-eta and WC-Co, as verified for a 12.1% WC-Co alloy at room temperature using a CALPHAD simulation. The VSM magnetic saturation results are consistent with carbon composition results in that the lower M_S leads to a higher carbon content. Despite the uncertainty in concluding whether or not eta phase exists, it can be seen that the ratio of W/C is very close to 1 for all three samples analyzed. This is a promising result that can offer slightly more certainty that there is likely no eta phase.

6.0 Conclusions and Future Work

The set of parameters that produced the highest sintered density was for Run 2. The subsequent characterization showed grain sizes between medium and coarse grained, hardness values within acceptable limits, toughness values above acceptable limits, a lower cobalt content than expected, and 1.029 W/C ratio. Additionally, there was no conclusive evidence for eta phase or graphite. Therefore, although not all properties were ideal, the Run 2 parameters produced a high-density part with properties that can be further tailored through an optimized sintering procedure to control grain growth, which will impact hardness and toughness.

Overall, this study showed that BJ3DP is a viable method for producing WC-Co parts. It was shown that the DOE method of screening is an efficient way of determining optimal properties for an industrial process. Additionally, contrary to the current literature, high densities and good mechanical properties are possible to achieve in BJ3DP WC-Co parts without using pre-sintered powder. This result is significant because it removes an entire step in the processing of BJ3DP WC-Co.

6.1 Response to Hypotheses

Hypothesis 2 was accepted in that DOE was successfully used to develop a set of parameters was determined for optimal green and sintered densities. The parameters of Run 2 were determined to be optimal for the BJ3DP of WC-Co:

- Layer Thickness: 100 μm
- Roller Traverse Speed: 5 mm/s

- Feed Ratio: 2
- Dry Time: 45 s
- Binder Saturation: 200% (100% for accurate powder packing rate)

Hypothesis 1a, b, and c are all accepted on the basis that the averages of grain size, density, and hardness were all within reasonable ranges for the optimized set of parameters.

Hypothesis 1d was rejected due to the high toughness values obtained for all samples.

6.2 Future Work

This study lays the groundwork for future studies in the BJ3DP of WC-Co. More work must be done to further tailor the final properties of the parts as well as surface finish and green part strength. These areas of improvement can be addressed in the following ways:

- Due to the nature of BJ3DP being different than traditional powder metallurgy processes, the sintering parameters can be studied to further optimize the density and mechanical properties of the BJ3DP. This will give a broader understanding of the mechanisms at work and how the printing effects sintering parameters and vice versa.
- It is necessary to study the BJ3DP of WC-Co using a printhead that is capable of higher resolution prints. A smaller droplet volume would allow for a reduced layer thickness and better surface finish.
- A few studies have recently been exploring the use of nanoparticle-binder suspensions during printing. This method loads metal nanoparticles into the printer binder to fill voids during printing, increasing green strength and reducing the amount of deformation that occurs during sintering. It would be of interest to study the addition

of cobalt nanoparticles into the binder for WC-Co. Some experiments are currently being carried out to study this area of technology, but not enough work has been completed to include the results in this study.

Bibliography

[1] J. García, V. Collado Ciprés, A. Blomqvist, and B. Kaplan, "Cemented carbide microstructures: a review," *International Journal of Refractory Metals and Hard Materials,* vol. 80, pp. 40-68, 2019, doi: 10.1016/j.ijrmhm.2018.12.004.

[2] C. L. Cramer *et al.*, "Binder jet printed WC infiltrated with pre-made melt of WC and Co," *International Journal of Refractory Metals and Hard Materials,* vol. 87, 2020, doi: 10.1016/j.ijrmhm.2019.105137.

[3] C. L. Cramer, P. Nandwana, R. A. Lowden, and A. M. Elliott, "Infiltration studies of additive manufacture of WC with Co using binder jetting and pressureless melt method," *Additive Manufacturing,* vol. 28, pp. 333-343, 2019, doi: 10.1016/j.addma.2019.04.009.

[4] A. Y. Kumar, Y. Bai, A. Eklund, and C. B. Williams, "The effects of Hot Isostatic Pressing on parts fabricated by binder jetting additive manufacturing," *Additive Manufacturing,* vol. 24, pp. 115-124, 2018, doi: 10.1016/j.addma.2018.09.021.

[5] A. Mostafaei *et al.*, "Binder jet 3D printing – Process parameters, materials, properties, and challenges," *Progress in Materials Science,* 2020, doi: 10.1016/j.pmatsci.2020.100707.

[6] R. K. Enneti, R. Morgan, and S. V. Atre, "Effect of process parameters on the Selective Laser Melting (SLM) of tungsten," *International Journal of Refractory Metals and Hard Materials,* vol. 71, pp. 315-319, 2018, doi: 10.1016/j.ijrmhm.2017.11.035.

[7] R. K. Enneti and K. C. Prough, "Effect of binder saturation and powder layer thickness on the green strength of the binder jet 3D printing (BJ3DP) WC-12%Co powders," *International Journal of Refractory Metals and Hard Materials,* vol. 84, 2019, doi: 10.1016/j.ijrmhm.2019.104991.

[8] R. K. Enneti and K. C. Prough, "Wear properties of sintered WC-12%Co processed via Binder Jet 3D Printing (BJ3DP)," *International Journal of Refractory Metals and Hard Materials,* vol. 78, pp. 228-232, 2019, doi: 10.1016/j.ijrmhm.2018.10.003.

[9] R. K. Enneti, K. C. Prough, T. A. Wolfe, A. Klein, N. Studley, and J. L. Trasorras, "Sintering of WC-12%Co processed by binder jet 3D printing (BJ3DP) technology," *International Journal of Refractory Metals and Hard Materials,* vol. 71, pp. 28-35, 2018, doi: 10.1016/j.ijrmhm.2017.10.023.

[10] N. Ku, J. J. Pittari, S. Kilczewski, and A. Kudzal, "Additive Manufacturing of Cemented Tungsten Carbide with a Cobalt-Free Alloy Binder by Selective Laser Melting for High-Hardness Applications," *Jom,* vol. 71, no. 4, pp. 1535-1542, 2019, doi: 10.1007/s11837-019-03366-2.

[11] L. Fu, L. H. Cao, and Y. S. Fan, "Two-step synthesis of nanostructured tungsten carbide-cobalt powders," *Scripta Materialia,* vol. 44, pp. 1061-1068, 2001, doi: 10.1016/S1359-6462(01)00668-6.

[12] C. M. Fernandes *et al.*, "Mechanical characterization of WC–10 wt% AISI 304 cemented carbides," *Materials Science and Engineering: A,* vol. 618, pp. 629-636, 2014, doi: 10.1016/j.msea.2014.09.064.

[13] D. Thakur, B. Ramamoorthy, and L. Vijayaraghavan, "Influence of different post treatments on tungsten carbide–cobalt inserts," *Materials Letters,* vol. 62, no. 28, pp. 4403-4406, 2008, doi: 10.1016/j.matlet.2008.07.043.

[14] Y. Wu, J. Dang, Z. Lv, and R. Zhang, "The preparation of tungsten carbides and tungsten powders by reaction of tungsten trioxide with methanol," *International Journal of Refractory Metals and Hard Materials,* vol. 76, pp. 99-107, 2018, doi: 10.1016/j.ijrmhm.2018.06.002.

[15] A. S. Kurlov and A. I. Gustev, *Tungsten Carbides: Structure, Properties and Application in Hardmetals* (Springer Series in Materials Science). Switzerland: Springer International Publishing, 2013.

[16] M. He, J. Wang, R. He, H. Yang, and J. Ruan, "Effect of cobalt content on the microstructure and mechanical properties of coarse grained WC-Co cemented carbides fabricated from chemically coated composite powder," *Journal of Alloys and Compounds,* vol. 766, pp. 556-563, 2018, doi: 10.1016/j.jallcom.2018.06.366.

[17] S. Guo, F. Yu, Y. Zhou, J. Yang, and H. Chen, "Investigation on reduction and carbonization process of WC-Co composite powder obtained by In situ synthesis," *Journal of Alloys and Compounds,* vol. 775, pp. 1086-1093, 2019, doi: 10.1016/j.jallcom.2018.10.211.

[18] F. L. Zhang, C. Y. Wang, and M. Zhu, "Nanostructured WC/Co composite powder prepared by high energy ball milling," *Scripta Materialia,* vol. 49, no. 11, pp. 1123-1128, 2003, doi: 10.1016/j.scriptamat.2003.08.009.

[19] R. M. Raihanuzzaman, T. S. Jeong, R. Ghomashchi, Z. Xie, and S.-J. Hong, "Characterization of short-duration high-energy ball milled WC–Co powders and subsequent consolidations," *Journal of Alloys and Compounds,* vol. 615, pp. S564-S568, 2014, doi: 10.1016/j.jallcom.2013.12.104.

[20] H. Lin, J. Sun, C. Li, H. He, L. Qin, and Q. Li, "A facile route to synthesize WC–Co nanocomposite powders and properties of sintered bulk," *Journal of Alloys and Compounds,* vol. 682, pp. 531-536, 2016, doi: 10.1016/j.jallcom.2016.03.285.

[21] H. Wang, Q. Qiu, M. Gee, C. Hou, X. Liu, and X. Song, "Wear resistance enhancement of HVOF-sprayed WC-Co coating by complete densification of starting powder," *Materials & Design,* vol. 191, 2020, doi: 10.1016/j.matdes.2020.108586.

[22] I. Borgh *et al.*, "Microstructure, grain size distribution and grain shape in WC–Co alloys sintered at different carbon activities," *International Journal of Refractory Metals and Hard Materials,* vol. 43, pp. 205-211, 2014, doi: 10.1016/j.ijrmhm.2013.12.007.

[23] V. K. Sarin, "Morphology of ETA phase in cemented WC-Co alloys," *Modern Developments in Powder Metallurgy,* vol. 10, pp. 553-565, 1977.

[24] M. Brieseck, W. Lengauer, B. Gneiß, K. Wagner, and S. Wagner, "A straightforward method for analysing the grain-size distribution in tungsten carbide - cobalt hardmetals," *Microchimica Acta,* vol. 168, no. 3-4, pp. 309-316, 2010, doi: 10.1007/s00604-010-0294-4.

[25] B. Roebuck and E. G. Bennett, "Phase Size Distribution in WC/Co Hardmetal," *Metallography,* vol. 19, pp. 27-47, 1986, doi: 10.1016/0026-0800(86)90005-4.

[26] J. Weidow, E. Olsson, and H.-O. Andrén, "Chemistry of binder phase grain boundary in WC–Co based cemented carbide," *International Journal of Refractory Metals and Hard Materials,* vol. 41, pp. 366-369, 2013, doi: 10.1016/j.ijrmhm.2013.05.011.

[27] W. D. Schubert, H. Neumeister, G. Kinger, and B. Lux, "Hardness to toughness relationship of fine-grained WC-CO hardmetals," *International Journal of Refractory Metals and Hard Materials,* vol. 16, pp. 133-142, 1998, doi: 10.1016/S0263-4368(98)00028-6.

[28] R. Furushima *et al.*, "Relationship between hardness and fracture toughness in WC–FeAl composites fabricated by pulse current sintering technique," *International Journal of Refractory Metals and Hard Materials,* vol. 42, pp. 42-46, 2014, doi: 10.1016/j.ijrmhm.2013.10.008.

[29] M. M. Karimi, U. U. Gomes, M. P. Oliveira, R. D. S. Guimarães, M. M. B. Mello, and M. Filgueira, "Fracture toughness evaluation of WC–10 wt% Co hardmetal sintered under high pressure and high temperature," *High Pressure Research,* vol. 37, no. 1, pp. 59-69, 2016, doi: 10.1080/08957959.2016.1261403.

[30] Y. Zhang, P. Xu, C. Liu, J. Ren, and H. Gong, "The influence of carbides on the microstructure, grain growth, and oxidation resistance of nanostructured carbides-strengthened cobalt-based multi-track laser-cladding layers," *Applied Surface Science,* vol. 469, pp. 495-504, 2019, doi: 10.1016/j.apsusc.2018.11.084.

[31] N. Lin, Y. He, C. Wu, Q. Zhang, J. Zou, and Z. Zhao, "Fabrication of tungsten carbide–vanadium carbide core–shell structure powders and their application as an inhibitor for the sintering of cemented carbides," *Scripta Materialia,* vol. 67, no. 10, pp. 826-829, 2012, doi: 10.1016/j.scriptamat.2012.07.043.

[32] N. A. N. Balbino, E. O. Correa, and L. de Carvalho Valeriano, "Development of the 90WC-8Ni-2Cr3C2 cemented carbide for engineering applications," *The International Journal of Advanced Manufacturing Technology,* vol. 99, no. 5-8, pp. 1653-1660, 2018, doi: 10.1007/s00170-018-2511-y.

[33] J. Gurland, "A Study of the Effects of Carbon Content on the Sturcture and Properties of Sintered WC-Co Alloys," *Journal of Metals,* vol. 6, pp. 285-290, 1954.

[34] Y. Gao *et al.*, "Mechanical properties and microstructure of WC-Fe-Ni-Co cemented carbides prepared by vacuum sintering," *Vacuum,* vol. 143, pp. 271-282, 2017, doi: 10.1016/j.vacuum.2017.06.028.

[35] R. K. Viswanadham and P. G. Lindquist, "Transformation-Toughening in Cemented Carbides: Part I. Binder Composition Control," *Metallurgical Transactions A,* vol. 18A, pp. 2163-2173, 1987.

[36] O. J. Ojo-kupoluyi, S. M. Tahir, M. A. Azmah Hanim, B. T. H. T. Baharudin, K. A. Matori, and M. S. Anuar, "Role of carbon addition on the microstructure and mechanical properties of cemented tungsten carbide and steel bilayer," *The International Journal of Advanced Manufacturing Technology,* vol. 92, no. 9-12, pp. 3363-3371, 2017, doi: 10.1007/s00170-017-0287-0.

[37] J. Li, J. Cheng, P. Chen, W. Chen, and C. Wei, "Fabrication of WC-Co cemented carbides with gradient distribution of WC grain size and Co composition by lamination pressing and microwave sintering," *Ceramics International,* vol. 44, pp. 11225-11232, 2018, doi: 10.1016/j.ceramint.2018.03.162.

[38] Y. Yuan, J. Ding, Y. Wang, and W. Sun, "Fabrication of functionally gradient ultrafine-grained WC-Co composites," *Applied Mechanics and Materials,* vol. 423-426, pp. 885-889, 2013, doi: 10.4028/www.scientific.net/AMM.423-426.885.

[39] C. B. Pollock and H. H. Stadelmaier, "The Eta Carbides In The Fe-W-C and Co-W-C Systems," *Metallurgical Transactions,* vol. 1, pp. 767-770, 1970, doi: 10.1007/BF02811752.

[40] K. H. Cho, J. W. Lee, and I. S. Chung, "A study on the formation of anomalous large we grain and the eta phase," *Materials Science and Engineering A,* vol. 209, pp. 298-301, 1996, doi: 10.1016/0921-5093(95)10104-7.

[41] G.-H. Lee and S. Kang, "Sintering of nano-sized WC–Co powders produced by a gas reduction–carburization process," *Journal of Alloys and Compounds,* vol. 419, no. 1-2, pp. 281-289, 2006, doi: 10.1016/j.jallcom.2005.09.060.

[42] A. Formisano, F. Capece Minutolo, A. Caraviello, L. Carrino, M. Durante, and A. Langella, "Influence of Eta-Phase on Wear Behavior of WC-Co Carbides," *Advances in Tribology,* vol. 2016, pp. 1-6, 2016, doi: 10.1155/2016/5063274.

[43] X. Cai, L. Zhong, Y. Xu, X. Li, and M. Liu, "Microstructure and fracture toughness of a WC-Fe cemented carbide layer produced by a diffusion-controlled reaction," *Surface and Coatings Technology,* vol. 357, pp. 784-793, 2019, doi: 10.1016/j.surfcoat.2018.10.096.

[44] R. O. Ritchie, "The conflicts between strength and toughness," *Nat Mater,* vol. 10, no. 11, pp. 817-22, Oct 24 2011, doi: 10.1038/nmat3115.

[45] J. J. Roa *et al.*, "Intrinsic hardness of constitutive phases in WC–Co composites: Nanoindentation testing, statistical analysis, WC crystal orientation effects and flow stress for the constrained metallic binder," *Journal of the European Ceramic Society,* vol. 35, no. 13, pp. 3419-3425, 2015, doi: 10.1016/j.jeurceramsoc.2015.04.021.

[46] L. A. Hanner, J. J. Pittari, and J. J. Swab, "Dynamic hardness of cemented tungsten carbides," *International Journal of Refractory Metals and Hard Materials,* vol. 75, pp. 294-298, 2018, doi: 10.1016/j.ijrmhm.2018.05.007.

[47] D. K. Shetty, I. G. Wright, P. N. Mincer, and A. H. Clauer, "Indentation fracture of WC-Co cermets," *Journal of Materials Science,* vol. 20, pp. 1873-1882, 1985, doi: 10.1007/BF00555296.

[48] T. A. Fabijanić, D. Ćorić, M. Šnajdar Musa, and M. Sakoman, "Vickers Indentation Fracture Toughness of Near-Nano and Nanostructured WC-Co Cemented Carbides," *Metals,* vol. 7, no. 4, 2017, doi: 10.3390/met7040143.

[49] R. Spiegler, S. Schmauder, and L. S. Sigl, "Fracture Toughness Evaluation of WC-Co Alloys by Indentation Testing," *Journal of Hard Materials,* vol. 1, pp. 147-158, 1999.

[50] S. S. Ponomarev, A. V. Shatov, A. A. Mikhailov, and S. A. Firstov, "Carbon distribution in WC based cemented carbides," *International Journal of Refractory Metals and Hard Materials,* vol. 49, pp. 42-56, 2015, doi: 10.1016/j.ijrmhm.2014.08.001.

[51] D. Linder *et al.*, "A comparative study of microstructure and magnetic properties of a Ni Fe cemented carbide: Influence of carbon content," *International Journal of Refractory Metals and Hard Materials,* vol. 80, pp. 181-187, 2019, doi: 10.1016/j.ijrmhm.2019.01.014.

[52] I. Topić, H. G. Sockel, P. Wellmann, and M. Göken, "The influence of microstructure on the magnetic properties of WC/Co hardmetals," *Materials Science and Engineering: A,* vol. 423, no. 1-2, pp. 306-312, 2006, doi: 10.1016/j.msea.2006.02.018.

[53] A. Love, S. Luyckx, and N. Sacks, "Quantitative relationships between magnetic properties, microstructure and composition of WC–Co alloys," *Journal of Alloys and Compounds,* vol. 489, no. 2, pp. 465-468, 2010, doi: 10.1016/j.jallcom.2009.09.087.

[54] Z. Baojun, Q. Xuanhui, and T. Ying, "Powder injection molding of WC–8%Co tungsten cemented carbide," *International Journal of Refractory Metals and Hard Materials,* vol. 20, pp. 389-394, 2002, doi: 10.1016/S0263-4368(02)00015-X.

[55] M. Youseffi and I. A. Menzies, "Injection Moulding of WC–6Co Powder Using Two New Binder Systems Based on Montanester Waxes and Water Soluble Gelling Polymers," *Powder Metallurgy,* vol. 40, pp. 62-65, 1997.

[56] M. T. Martyn and P. J. James, "The Processingof Hardmetal Componentsby Powder Injection Moulding," *International Journal of Refractory Metals and Hard Materials,* vol. 12, pp. 61-69, 1993-1994.
[57] H. V. Atkinson and S. Davies, "Fundamental Aspects of Hot Isostatic Pressing: An Overview," *Metallurgical and Materials Transactions A,* vol. 31, pp. 2981-3000, 2000, doi: 10.1007/s11661-000-0078-2.
[58] D. Mari, L. Miguel, and C. E. Nebel, *Comprehensive Hard Materials*. Elsevier Science, 2014.
[59] M. Ziaee and N. B. Crane, "Binder jetting: A review of process, materials, and methods," *Additive Manufacturing,* vol. 28, pp. 781-801, 2019, doi: 10.1016/j.addma.2019.05.031.
[60] E. Uhlmann, A. Bergmann, and W. Gridin, "Investigation on Additive Manufacturing of Tungsten Carbide-cobalt by Selective Laser Melting," *Procedia CIRP,* vol. 35, pp. 8-15, 2015, doi: 10.1016/j.procir.2015.08.060.
[61] S. Kumar, "Manufacturing of WC–Co moulds using SLS machine," *Journal of Materials Processing Technology,* vol. 209, no. 8, pp. 3840-3848, 2009, doi: 10.1016/j.jmatprotec.2008.08.037.
[62] Y. Wang and Y. F. Zhao, "Investigation of Sintering Shrinkage in Binder Jetting Additive Manufacturing Process," *Procedia Manufacturing,* vol. 10, pp. 779-790, 2017, doi: 10.1016/j.promfg.2017.07.077.
[63] N. B. Crane, "Impact of part thickness and drying conditions on saturation limits in binder jet additive manufacturing," *Additive Manufacturing,* vol. 33, 2020, doi: 10.1016/j.addma.2020.101127.
[64] P. Nandwana, A. M. Elliott, D. Siddel, A. Merriman, W. H. Peter, and S. S. Babu, "Powder bed binder jet 3D printing of Inconel 718: Densification, microstructural evolution and challenges☆," *Current Opinion in Solid State and Materials Science,* vol. 21, no. 4, pp. 207-218, 2017, doi: 10.1016/j.cossms.2016.12.002.
[65] S. Shrestha and G. Manogharan, "Optimization of Binder Jetting Using Taguchi Method," *Jom,* vol. 69, no. 3, pp. 491-497, 2017, doi: 10.1007/s11837-016-2231-4.
[66] B. Utela, D. Storti, R. Anderson, and M. Ganter, "A review of process development steps for new material systems in three dimensional printing (3DP)," *Journal of Manufacturing Processes,* vol. 10, no. 2, pp. 96-104, 2008, doi: 10.1016/j.jmapro.2009.03.002.
[67] O. Eso, Z. Fang, and A. Griffo, "Liquid phase sintering of functionally graded WC–Co composites," *International Journal of Refractory Metals and Hard Materials,* vol. 23, no. 4-6, pp. 233-241, 2005, doi: 10.1016/j.ijrmhm.2005.04.017.
[68] J. Antony, *Design of Experiments for Engineers and Scientists*, Second Edition ed. Elsevier, 2014.
[69] *B213-20 Standard Test Method for Flow Rate of Metal Powders Using the Hall Flowmeter Funnel*, A. International, West Conshohocken, PA, 2020.
[70] M. Ziaee, E. M. Tridas, and N. B. Crane, "Binder-Jet Printing of Fine Stainless Steel Powder with Varied Final Density," *Jom,* vol. 69, no. 3, pp. 592-596, 2017, doi: 10.1007/s11837-016-2177-6.
[71] A. B. Spierings, M. Schneider, and R. Eggenberger, "Comparison of density measurement techniques for additive manufactured metallic parts," *Rapid Prototyping Journal,* vol. 17, no. 5, pp. 380-386, 2011, doi: 10.1108/13552541111156504.

[72] C. A. Schneider, W. S. Rasband, and K. W. Eliceiri, "NIH Image to ImageJ: 25 years of image analysis," *Nature Methods*, vol. 9, no. 7, pp. 671-675, Jul 2012, doi: 10.1038/nmeth.2089.
[73] J. W. Carson and B. H. Pittenger, "Bulk Properties of Powders," in *ASM Handbook, Volume 7: Powder Metal Technologies and Applications*, P. W. Lee *et al.* Eds.: ASM International, 1998, pp. 287-301.
[74] *The Designer's Guide to Tungsten Carbide*. (2015). General Carbide.